J. metamorphic Geol., 2006, **24,** 33–53 doi:10.1111/j.1525-1314.2005.00620.x

Deformation and fluid flow during orogeny at the palaeo-Pacific active margin of Gondwana: the Early Palaeozoic Robertson Bay accretionary complex (north Victoria Land, Antarctica)

F. ROSSETTI[1], F. TECCE[2], L. ALDEGA[1], M. BRILLI[2] AND C. FACCENNA[1]
[1]*Dipartimento di Scienze Geologiche, Università ROMA TRE, 00146 Rome, Italy (rossetti@uniroma3.it)*
[2]*Istituto di Geologia Ambientale e Geoingegneria, CNR, 00185 Rome, Italy*

ABSTRACT Structural investigations, integrated with X-ray diffraction, fluid inclusion microthermometry and oxygen-stable isotope analyses are used to reconstruct the deformation history and the palaeo-fluid circulation during formation of the low-grade, turbidite-dominated Early Palaeozoic Robertson Bay accretionary complex of north Victoria Land (Antarctica). Evidence for progressive deformation is elucidated by analysing the textural fabric of chronologically distinct, thrust-related quartz vein generations, incrementally developed during progressive shortening and thickening of the Robertson Bay accretionary complex. Our data attest that orogenic deformation was mainly controlled by dissolution–precipitation creep, modulated by stress- and strain-rate-dependent fluid pressure cycling, associated with local and regional permeability variations induced by the distribution and evolution of the fracture network during regional thrusting. Fracture-related fluid pathways constituted efficient conduits for episodic fluid flow. The dominant migrating fluid was pre-to-syn-folding and associated with the migration of warm (160–200 °C) nitrogen- and carbonic (CO_2 and CH_4)-bearing fluids. Both fluid advection and diffusive mass transfer are recognized as operative mechanisms for fluid–rock interaction and vein formation during continuous shortening. In particular, fluid–rock interaction was the consequence of dissolution–precipitation creep assisted by tectonically driven cooling fluids moving through the rock section as a result of seismic pumping. The most likely source of the migrating fluids would be the frontal part of the growing accretionary complex, where fluids from the deep levels in the hinterland are driven trough channelization operated by the thrust-related fracture (fault) systems.

Key words: accretionary complex; Antarctica; Early Palaeozoic; fluid flow; north Victoria Land; thermobarometry.

INTRODUCTION

Both modern and ancient examples of accretionary complexes provide outstanding examples of faulting experienced during high fluid-flow regimes (e.g. Vrolijk, 1987; Cox, 1995; Fisher *et al*., 1995; Fisher, 1996). The large volume of fluid is derived from sediments entering accretionary complexes at convergent plate margins, which is rapidly expulsed during progressive compaction because of tectonic loading (Vrolijk, 1987; Saffer & Bekins, 1999). Key evidence for high fluid pressure accompanying orogenic complex formation is provided by the widespread development of vein arrays, which commonly formed by extension hydrofracturing (Etheridge *et al*., 1984). Vein opening provided fluid-flow pathways resulting in the release of the fluid overpressure (fluid pressure in excess of the lithostatic load, i.e. $P > \sigma_3$), which has been demonstrated to be transient and fluctuating – a consequence of the pumping effect induced by the development of thrusts and folds during continuous shortening (Sibson *et al*., 1975, 1988; Byerlee, 1993; Cosgrove, 1993; Cox, 1995; Fisher, 1996; Henderson & McCaig, 1996; Sibson, 2004).

In siliciclastic sequences, the veins are commonly dominated by quartz (e.g. Gray *et al*., 1991; Fisher, 1996) and pressure drop upon hydrofracturing is usually advocated as the main mechanism for Si precipitation, although cooling of quartz-bearing fluid has also been taken into account (Bons, 2001 and references therein). Regardless of the process promoting Si precipitation in veins, it is crucial to understand the fluid regimes responsible for vein formations, i.e. close or open fluid circulation systems (e.g. Oliver, 1996; Cartwright & Buick, 2001; Richards *et al*., 2002). This may have important consequences in defining the scale of the fluid–rock interaction and its impact in controlling rheological properties during orogenic complex formation (e.g. Stöckert *et al*., 1999; Goldstein *et al*., 2005).

In this paper, after revisiting the metamorphic conditions of the Early Palaeozoic Robertson Bay Terrane of north Victoria Land in East Antarctica (Findlay, 1986; GANOVEX Team, 1987; Fig. 1), we focused the

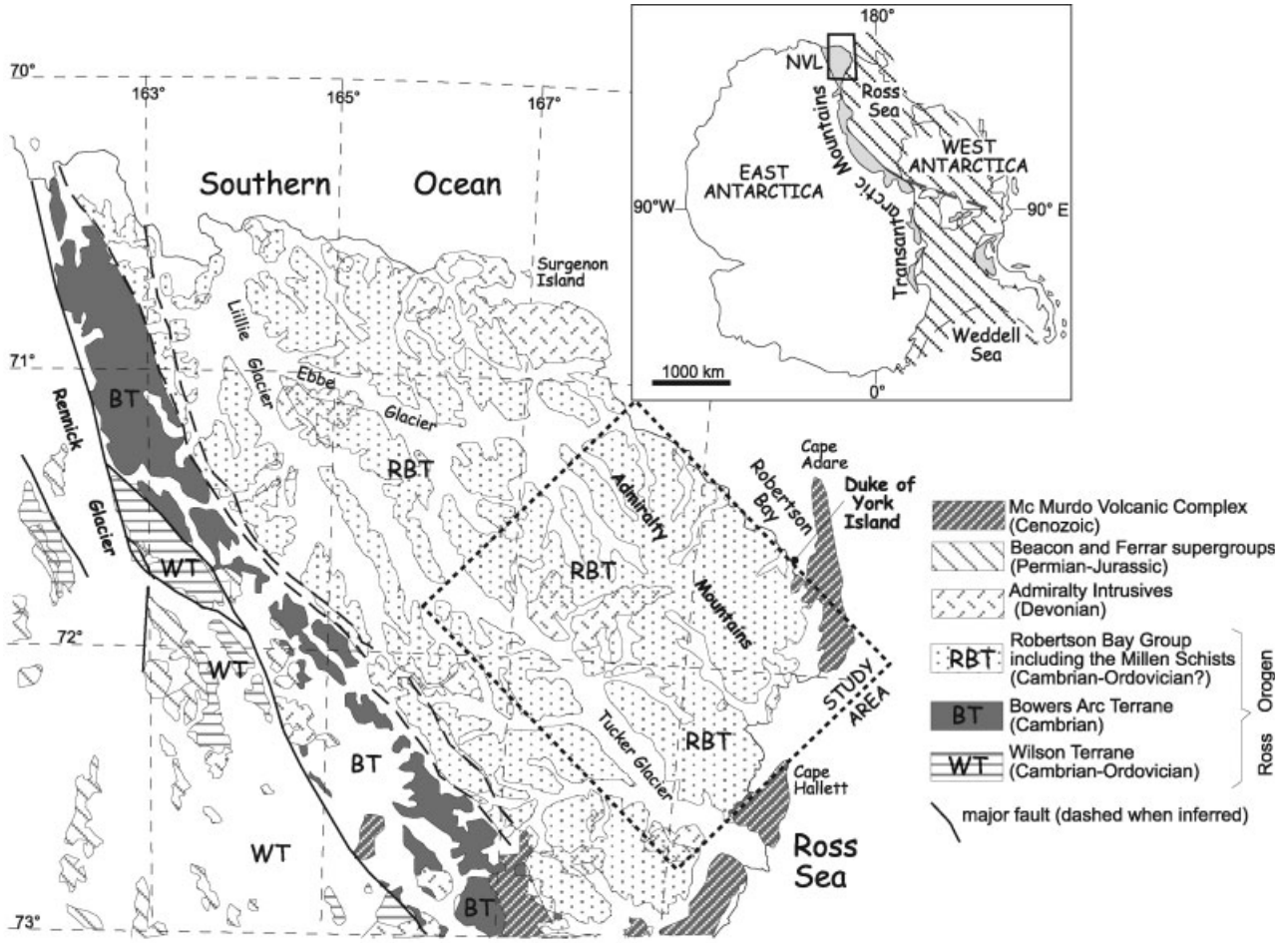

Fig. 1. Geological sketch map of north Victoria Land, with the main lithotectonic units indicated (modified and re-adapted after GANOVEX Team, 1987). The study area is shown.

study on distinct generations of quartz veins, which are interpreted to record the incremental deformation history during thrusting and accretionary complex formation at the palaeo-Pacific margin of Gondwana. Samples from both the host rocks and the vein materials were collected in different structural settings and properly selected for microstructural, fluid-inclusion microthermometric, petrographical and stable-isotope analyses in order to elucidate the deformation process, the fluid–rock interactions and the scale of fluid flow during orogenic complex formation. The results obtained from this study provide clues to the tectonothermal history and inferences on the palaeo-fluid circulation associated with orogenic construction at the palaeo-Pacific active margin of Gondwana.

THE ROSS OROGEN IN NORTH VICTORIA LAND

The Early Palaeozoic tectonic evolution of the Pacific margin of Gondwana has been classically referred to the development of a convergent plate boundary during the Cambrian–Ordovician Delamerian/Ross orogeny. The remnants of this formerly continuous belt are now exposed in SE Australia and northern Victoria Land in East Antarctica, recording similar tectonic histories (Flöttmann *et al*., 1993).

In north Victoria Land, three major NW-trending terranes, Neoproterozoic to Early Palaeozoic in age, are generally recognized (e.g. Gair *et al*., 1969; Bradshaw *et al*., 1985; GANOVEX Team, 1987; Kleinschmidt & Tessensohn, 1987); from west to east these are: the Wilson, Bowers and Robertson Bay terranes (Fig. 1). The Wilson terrane is characterized by low- to high-grade metamorphic rocks, hosting syn- to post-tectonic Cambrian–Ordovician granitoid bodies of the Granite Harbour Intrusives. The Bowers Terrane consists of a sequence of low-grade metamorphosed volcanic rocks and proximal marine volcanoclastic rocks of Middle Cambrian age. The Robertson Bay Terrane is the most areally extensive tectono-stratigraphic domain and consists of thick and laterally homogeneous sequence of folded and imbricated anchizonal to low greenschist facies metasediments (the Robertson Bay Group rocks). The protoliths of this

thick rock succession consists of quartz-dominated turbidite and slates of the Robertson Bay Group deposited in a fan to basin-plain environment. The uppermost portions of this sequence range in age from the uppermost Cambrian to lowermost Ordovician (GANOVEX Team, 1987). The post-tectonic emplacement of the Admiralty Intrusives suite, Devonian–Carboniferous in age (Fioretti *et al.*, 1997 and references therein) post-dated the Ross orogenic signature in north Victoria Land (Fig. 1).

There is increasing consensus in considering the terrane model of north Victoria Land as a fossil arc–trench system linked to a westward-directed subduction system at the palaeo-Pacific active margin of Gondwana during the Ross/Delamerian orogeny (e.g. Kleinschmidt & Tessensohn, 1987; Ricci *et al.*, 1997; Finn *et al.*, 1999; Ferraccioli *et al.*, 2002 and references therein). In this configuration, the Wilson, Bowers and Robertson Bay terranes represent the roots of the continental margin magmatic arcs, the forearc and the trench sedimentary sequences respectively (Finn *et al.*, 1999). Recently, Roland *et al.* (2004) provided a new scenario for the reconstruction of the palaeo-Pacific active margin of Gondwana framed within a subduction–collision tectonic setting, where collision and docking of an allochthonous island arc (Bowers Terrane) to the Wilson active margin of Gondwana was followed by the progressive retreat of the subduction zone and formation of the Robertson Bay accretionary complex, during continuous turbiditic sedimentation.

METAMORPHIC CONDITIONS IN THE ROBERTSON BAY TERRANE

In low-grade metamorphic rock successions such as those of the Robertson Bay Terrane (Kleinschmidt, 1983; Findlay, 1986; Buggish & Kleinschmidt, 1989), integration of illite crystallinity (IC) measurements and K-mica b_0 dimensions as determined by X-ray diffraction provides an effective tool to define the grade and baric conditions of metamorphism respectively (e.g. Frey & Robinson, 1999). Previous K-mica b_0 geobarometry on the Robertson Bay Group samples yielded a mean value of 9.026 Å (Kleinschmidt *et al.*, 1991), which is indicative of intermediate-pressure metamorphic conditions (Sassi & Scolari, 1974). The IC analyses carried out by Buggish & Kleinschmidt (1989) on the Robertson Bay Group samples provided values ranging between 0.12 and 0.20 (mean 0.13)°$\Delta 2\theta$, considered as indicative of a peak temperature of *c.* 250 °C. This data set, however, is not compatible with other data from the literature, because of the lack of an interlaboratory calibration procedure. By applying our linear regression equation (see Appendix), a mean IC value of 0.36°$\Delta 2\theta$ can be obtained.

We integrate these available data sets with a new pilot X-ray powder diffraction study for both quantitative analysis and IC measurements on 12 pelite samples (see Table 1 for sample localities). Illite and chlorite are the only minerals identified in both the < 2 μm (equivalent spherical diameter) and 2–16 μm grain-size fractions of the Robertson Bay Group samples. No mixed layers or expandable clays were found in the mixture. Ethylene–glycol solvation did not display any shift between the air-dried and the glycolated patterns. The X-ray diffraction peaks of the 10- and 14-Å minerals are very sharp and symmetrical, without traces of small amounts of interfering minerals in the peak tails (e.g. illite–smectite and/or chlorite–smectite mixed layers). X-ray quantitative results are shown in Table 2.

Table 1. Samples localities used for this study.

Sample	Locality	USGS-Sheet name	Latitude (°S)	Longitude (°E)	Lithology
CR4-10/01/02	Mount Finch	Cape Hallett	72°39′299″	167°23′512″	Quartz vein
CR6-10/01/02	Mount Finch	Cape Hallett	72°39′299″	167°23′512″	Quartz vein
CR1-11/01/02	Duke of York Island	Cape Adare	71°31′900″	170°01′098″	Quartz vein
CR2-11/01/02	Duke of York Island	Cape Adare	71°31′900″	170°01′098″	Quartz vein
CR3-11/01/02	Duke of York Island	Cape Adare	71°31′900″	170°01′098″	Quartz vein
CR4-11/01/02	Duke of York Island	Cape Adare	71°31′900″	170°01′098″	Metapelite
CR2a-12/01/02	Penelope Point	Cape Adare	71°30′381″	170°45′810″	Quartz vein
CR2a-12/01/02	Penelope Point	Cape Adare	71°30′381″	170°45′810″	Metapelite
CR3-12/01/02	Penelope Point	Cape Adare	71°30′381″	170°45′810″	Metapelite
CR4-12/01/02	Penelope Point	Cape Adare	71°30′381″	170°45′810″	Metapsammite
CR5-12/01/02	Penelope Point	Cape Adare	71°30′381″	170°45′810″	Metapsammite
CR6-12/01/02	Penelope Point	Cape Adare	71°30′381″	170°45′810″	Metapelite
CR1a-13/01/02	Luther Peak	Cape Hallett	72°22′432″	169°53′874″	Metapelite
CR1a-13/01/02	Luther Peak	Cape Hallett	72°22′432″	169°53′874″	Quartz vein
CR3-13/01/02	Luther Peak	Cape Hallett	72°22′432″	169°53′874″	Metapsammite
CR5-13/01/02	Mount McDonald	Cape Hallett	72°31′896″	166°44′579″	Metapelite
CR6-13/01/02	Mount McDonald	Cape Hallett	72°31′896″	166°44′579″	Metapsammite
CR7a-13/01/02	Handler Ridge	Cape Hallett	72°30′435″	167°12′728″	Metapelite
CR7b-13/01/02	Handler Ridge	Cape Hallett	72°30′435″	167°12′728″	Metapelite
CR1-17/01/02	Mount McDonald	Cape Hallett	72°31′141″	166°44′345″	Metapelite
CR8a-21/01/02	Inferno Peak	Freyberg Mountains	72°04′994″	166°05′639″	Quartz vein
CR8b-21/01/02	Inferno Peak	Freyberg Mountains	72°04′994″	166°05′639″	Metapelite
CR9-21/01/02	Inferno Peak	Freyberg Mountains	72°04′994″	166°05′639″	Quartz vein
CR2-24/01/02	Trainer Glacier	Cape Hallett	72°38′166″	167°167′365″	Quartz vein

Table 2. X-ray diffraction results.

	< 2 μm grain-size fraction	2–16 μm grain-size fraction		
Sample	Illite	Chlorite	Illite	Chlorite
CR1-13/01/02	77	23	68	32
CR1-17/01/02	65	35	48	52
CR2-12/01/02	68	32	60	40
CR3-12/01/02	79	21	63	37
CR3-13/01/02	74	26	79	21
CR4-11/01/02	69	31	58	42
CR4-12/01/02	70	30	64	36
CR5-12/01/02	68	32	54	46
CR5-13/01/02	80	20	57	43
CR6-13/01/02	66	34	52	48
CR7-13/01/02	77	23	56	44
CR9-21/01/02	77	23	56	44

Non-clay minerals were not taken into account in the normalized weight per cent.

Illite is the most abundant mineral with average values equal to 70% and 59% in the < 2 and 2–16 μm grain-size fractions respectively. Chlorite shows a relative increase of its weight per cent in the coarser fraction moving from 41% (< 2 μm) to 59%. Non-clay minerals such as quartz, plagioclase and calcite are also present in the oriented mounts, but they were not included in the quantitative analysis of the oriented aggregates. The chemical composition of chlorite can be determined by plotting the I(14 Å), I(7 Å) and I(4.7 Å) on the triangular diagram of Oinuma *et al.* (1972). Our data, relative to both the < 2 μm and the 2–16 μm grain-size fractions are indicative of enriched (Mg, Fe)-chlorite, with an excess of Fe in the silicate layer (field ABD in Fig. 2a). The chemical composition of the micaceous phases can be obtained from the Rey & Kübler (1983) diagram. The X-ray diffraction intensity of the harmonic series (0 0 l) measured on oriented preparations was corrected for both the intensity loss of the diffracted beam at the specific diffraction angles and for the sample thickness. Data fall between the illite and phengite composition, with a little compositional difference between the < 2 μm and the 2–16 μm grain-size fractions. The finer fraction shows a 10-Å phase of more phengite-like composition than the coarser one (Fig. 2b).

The IC data for illite are shown in Table 3. Pelites from the Robertson Bay Terrane are mostly anchizonal in grade, with an average IC value of $0.36 \pm 0.05°\Delta 2\theta$. Only sample CR1-13/01/02 has a higher IC value of $0.52°\Delta 2\theta$, indicative of the diagenetic zone. Accordingly, the IC mean value indicates that peak temperature conditions during burial of the Robertson Bay Group rocks were in the order of 200–250 °C (see Hoffman & Hower, 1979; Merriman & Kemp, 1996), confirming the results presented in Buggish & Kleinschmidt (1989).

Approximate burial pressure can be derived from the P–T–b_0 grid of Guidotti & Sassi (1986) by extending the b_0 curves into the sub-greenschist facies P–T space (Underwood *et al.*, 1993). Assuming a temperature range of 200–250 °C and an average b_0 value of 9.026 Å (Kleinschmidt *et al.*, 1991), a maximum pressure of *c.* 200 MPa can be estimated. This indicates a burial depth of *c.* 7 km (assuming a density of 2700 kg m^{-3} for the rocks) and a palaeogeothermal gradient of *c.* 25–30 °C km^{-1}. This is in agreement with the palaeotectonic setting of the Robertson Bay Group rocks that probably corresponded to the sedimentary infilling of a foredip basin, receiving sediments from the building thrust systems in the hinterland (Finn *et al.*, 1999; Roland *et al.*, 2004).

STRUCTURES IN THE ROBERTSON BAY TERRANE AND THE VEIN SYSTEMS

The deformation associated with formation of the Robertson Bay accretionary complex is related to the development of a fold-thrust belt, showing regional-scale regularity of NW–SE-trending, upright chevron folding (Kleindschmidt & Skinner, 1981; Findlay, 1986). The intensity of this deformation increases, moving towards the contact with the Bowers Terrane, marked by a continuous belt of highly deformed and mylonitized schists, known in the literature as the Millen Schists (Findlay, 1986; GANOVEX Team, 1987). The Robertson Bay Group rock successions are deformed into a steeply dipping, S1 pressure-solution foliation, which is axial planar to the regional-scale folding event (F1 in Findlay, 1986; Buggish & Kleinschmidt, 1989). The folded sequence is divided into thrust-bounded tectonic slices, where the F1 folds are continuous for tens of kilometres along strike and have wavelength of 200–300 m, with typical interlimb angles of ≤30° (Fig. 3a).

The Admiralty Mountain region facing the Robertson Bay area, located far east of the main tectonic boundary with the Bowers Terrane (Fig. 1), exposes a NW–SE-trending belt of rocks, where the transposition effects linked to thrusting deformation is less important. Overprinting relationships between the S1 foliation and the several generations of structures were used to establish an overall deformation chronology. Three main, centimetre-to-decimetre-thick, chronologically distinct generations of quartz vein systems (hereafter referred as category *a*, *b*, and *c*, respectively) were recognized in the field. The veins are largely composed of quartz, but occasionally contain minor calcite. Locally, the host rocks contain calcite immediately adjacent to the veins, as well as chlorite selvedges along the veins.

The early category *a* vein system consists of laminated quartz veins that occur folded and boudinaged along the S1 axial planar foliation (Fig. 3b,c). Category *b* vein system consists of bedding/foliation-parallel vein sets, usually associated with related extension cracks (Fig. 3d). The *c* vein system, the latest category, consists of shear zone-hosted quartz-laminated fault veins, which typically define the surfaces of moderately dipping, NW/SE-striking reverse, up to 1 cm thick, shear zones and faults. These fault veins

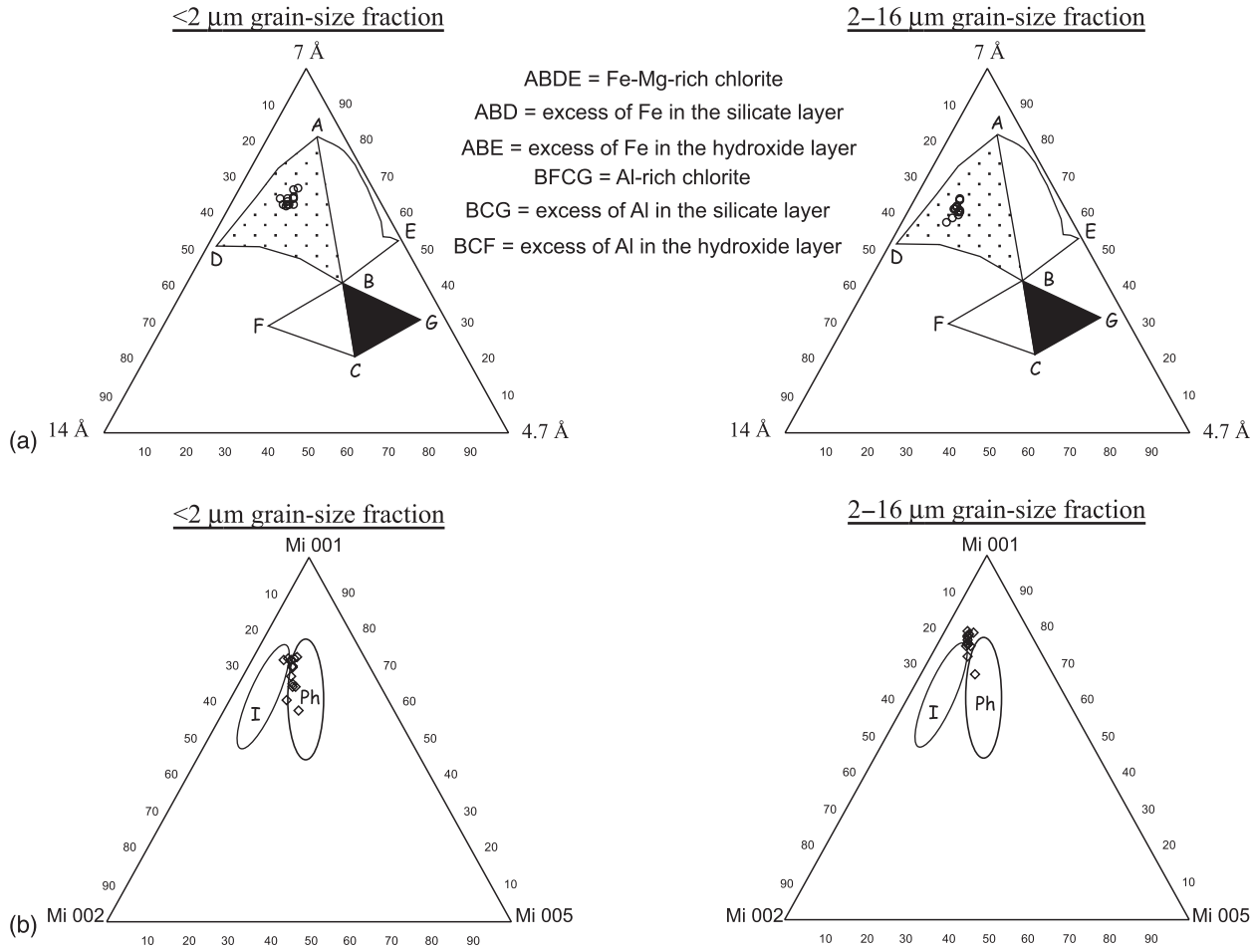

Fig. 2. (a) Chlorite compositions plotted on the triangular diagram of Oinuma *et al*. (1972). (b) Mica composition plotted on the triangular diagram of Rey & Kübler (1983). Vertexes represent the intensities of different (00*l*) XRD reflections. Data fall within the illite (I) and phengite (Ph) fields.

Table 3. Kübler index (IC) results.

Sample	<2 μm grain-size fraction		2–16 μm grain-size fraction Glycolated
	Air-dried	Glycolated	
CR1-13/01/02	0.52	0.54	0.4
CR1-17/01/02	0.34	0.34	0.33
CR2-12/01/02	0.36	0.36	0.32
CR3-12/01/02	0.34	0.34	0.34
CR3-13/01/02	0.35	0.35	0.35
CR4-11/01/02	0.32	0.32	0.32
CR4-12/01/02	0.36	0.36	0.34
CR5-12/01/02	0.31	0.31	0.31
CR5-13/01/02	0.34	0.34	0.34
CR6-13/01/02	0.41	0.39	0.34
CR7-13/01/02	0.35	0.34	0.32
CR9-21/01/02	0.37	0.35	0.35

have peculiar cross-cutting relationships with the main S1 foliation, being generally oblique to it and accommodating a dominant top-to-the-SW sense of shear (Fig. 3e).

The three categories of veins show linear features (quartz mineral fibres for categories *a* and *b*, and slickenside striations for category *c* veins; Fig. 3b,d), trending roughly orthogonal to the F1 axes and the axial planar S1 foliation (Fig. 3f). Finally, it is important to note that the category *a* composite vein arrays, analogous to that reported in Cosgrove (1993), are buckled along the large-scale folds (Fig. 3a–c). The disharmonic characters of the minor folds with respect to the wavelength of the regional folds indicate that segregation of the category *a* veins pre-dated the large-scale F1 folding event.

MICROSTRUCTURAL CHARACTERISTICS OF THE VEIN SYSTEMS

Oriented samples of the different vein generations (category *a*, *b* and *c*) were analysed at the thin-section scale in order to elucidate vein microstructures and to infer deformation mechanisms leading to vein development and overprinting relationships. All the descriptions of vein microstructures presented here pertain to thin section cut normal to the vein walls and parallel to the dominant lineation.

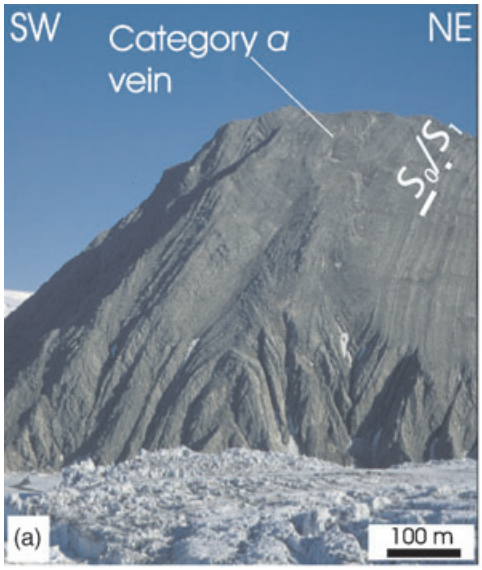

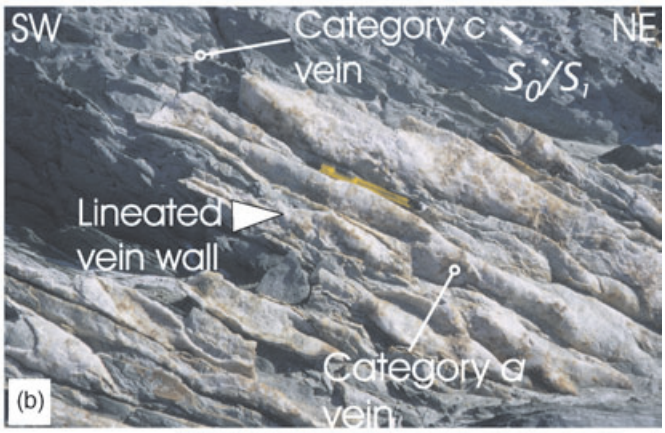

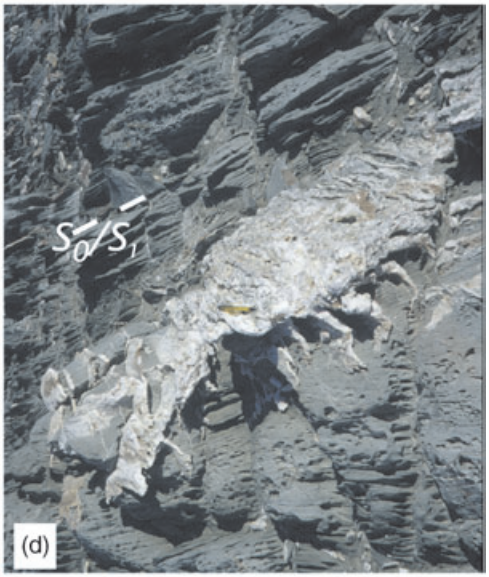

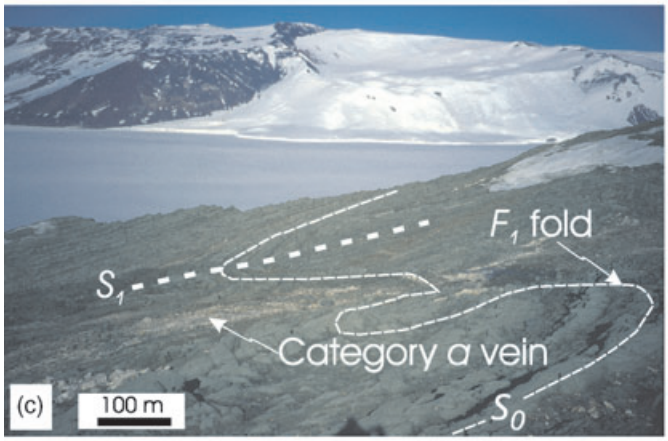

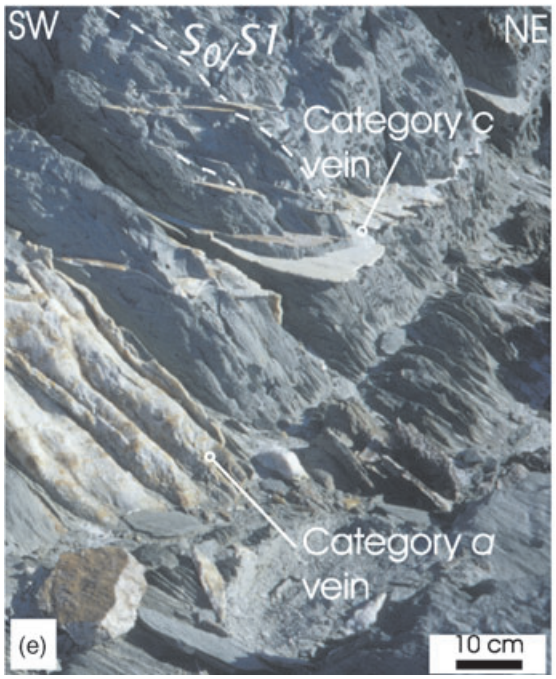

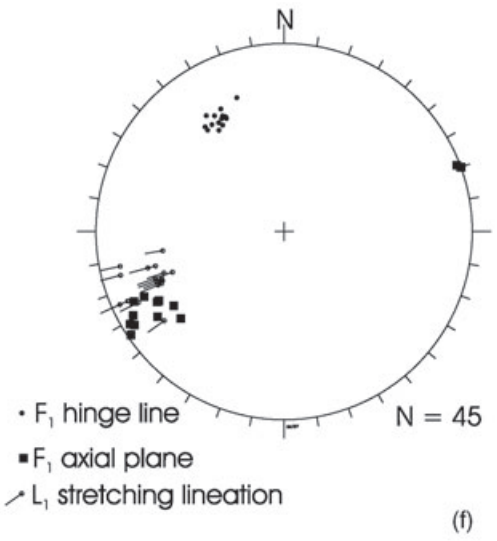

Category *a* veins

Category *a* veins are made up of layers of quartz crystals (0.25–1.5 mm in thickness), separated by thin-layer silicates (*c.* 10 μm thick). The quartz hosted in the veins reveals large grains with irregular shapes, which may be described as an overall blocky texture (Bons, 2000). Unaltered vein–host rock contacts are poorly preserved, as the veins systematically show collapsed morphologies because of the fact that the vein-to-wallrock interfaces acted as preferential sites for pressure-solution and removal of material during diffuse dissolution–precipitation creep and S1 crenulation cleavage development (Fig. 4a). The effects of dissolution–precipitation creep are also evident in the main body of the veins, where dissolution seam and stylolites mark sites of preferential removal of material (Fig. 4a). Further evidence for the operation of the dissolution–precipitation creep is provided by long grain contacts, truncations, grain-to-grain indentations and overgrowth (Fig. 4a).

Within the cleavage domains, a complex network of highly serrated stylolitic surfaces pervasively disrupt the quartz hosted in the veins, resulting in sutured intragranular contacts (Fig. 4b). Quartz microfabrics show no evidence of pervasive crystal-plastic deformation, as only few grains display patchy undulose extinction or low-angle grain boundaries. On the contrary, coarse-grained quartz grains typically show features resembling foam microstructure and diffuse microfracturing (Fig. 4c). In particular, fracturing occurred in two nearly orthogonal sets, which, oriented both orthogonal and parallel to the S1 surfaces, caused the quartz grains to be divided in a large number of fragments defining an overall polygonal microstructure (Fig. 4d). Clusters of small (from 10 to 100 μm in size) recrystallized quartz grains mainly occur along the hinge region of the F1 folds, where they occur as fragmentation halos bordering the highest stressed portions of pristine coarse-grained quartz grains mainly along the S1 cleavage surfaces (Fig. 4e).

Visible in some thin sections are dense arrays of solid and fluid inclusion bands along healed, microfracture trails at high angle to the stylolitized surfaces (Fig. 4f). Texturally late brecciation and fracturing of the quartz grain are also observed and calcite is found to be the typical mineral filling the voids both as euhedral crystals and cement (Fig. 4g). Twinning, kinking and fracturing of the calcite grain are systematically observed, in conjunction with distortion of the adjacent quartz grains, where moderate recovery processes are documented by the occurrence of subgrain formation and deformation lamellae (Fig. 4h).

Category *b* and *c* veins

Both veins of category *b* and *c* consist of planar arrays of laminae of quartz crystals, striking subparallel to the vein walls and alternating with slices of detached wallrock (Fig. 5a,b). Coarse-grained calcite grains are also commonly observed as vein-filling mineral, but are systematically observed either to straddle the boundaries of the quartz laminae or to constitute a polygonal mosaic of grains grown around the quartz grains (Fig. 5a). Furthermore, millimetric to submillimetric calcite veinlets are observed along the vein margins, clearly post-dating the vein–host rock interfaces. Chlorite is also systematically found in the region immediately adjacent the vein–host rock contacts (Fig. 5a).

Dissolution–precipitation creep intensively affects wallrock–vein interfaces and the vein margins, which are heavily stylolitized (Fig. 5b). However, in thin sections, the vein microstructure can be reconstructed. Quartz hosted in the veins dominantly consists of elongated blocky to stretched crystals (Bons, 2000 and references therein) with their long axis at low angle or parallel to vein walls. They have a variable thickness (from 50 μm to $\sim$1 cm), with high to extreme length/height ratios, frequently exceeding a value of 20. Typically, blocky textures of quartz are associated with regularly spaced trails of small inclusions bands (typically small mica or pieces of wallrock), indicating filling of the veins by the crack-seal mechanism (Ramsay, 1980; Fig. 5c).

The quartz microfabric of grains hosted in veins of category *b* and *c* is dominated by the effects produced by dissolution-precipitation creep. Healed intra- and transgranular fractures, marked by planar arrays of solid and fluid inclusions are common within the coarse grained quartz crystals, seldom overprinted by the development of the dissolution seams during main foliation development (Fig. 5d). This resulted in the formation of new recrystallized quartz grains, mostly localized along the strained region accommodating dissolution. These regions correspond to sites where plastic deformation of the

Fig. 3. (a) Typical upright F1 chevron folds affecting the Robertson Bay Group rocks (Duke of York Island area in Fig. 1, looking North). Category *a* veins are folded along the folds. (b) Minor folds affecting category *a* veins. Fold axes are approximately normal to the stretching lineations found on the vein surfaces. The geometrical relationships with the category *c* veins are also shown. (c) Plan view through the F1 fold trains shown in (a), showing the geometrical relationships between folding and veining. (d) Bedding-parallel category *b* veins in association with tension gashes departing from the main vein surface. (e) Flat-lying, category *c* shear veins cutting through the previously structured D1 fabric. The angular relationships between the vein set and the S0/S1 composite foliation points to a top-to-the-SW sense of shear (exposure normal to the shear vein and parallel to the lineations). (f) Stereoplot (Schmidt net, lower hemisphere) illustrating the geometric relationships between category *a* veins, lineations and F1 folding in the Robertson Bay area (Duke of York Island area in Fig. 1).

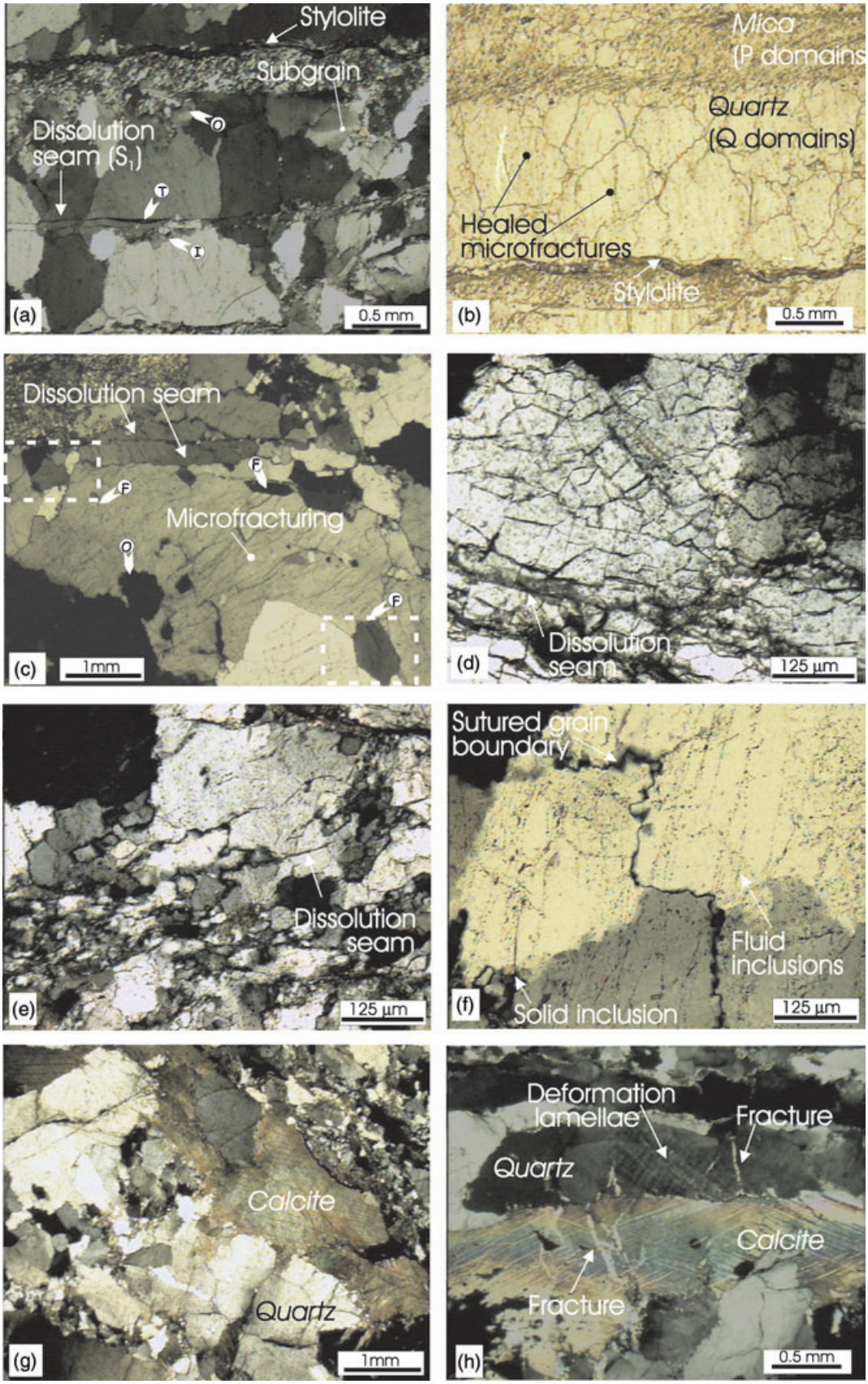

quartz grains also occurs, as attested by slight undulatory extinction (Fig. 5d).

Texturally late brecciation and fracturing of the previously sutured intragranular quartz contacts are commonly observed. This results in a background coarse porosity (size 10–20 μm), usually healed by calcite segregation, which commonly constitutes the cement filling the voids (Fig. 5e). Calcite cement is usually fine-grained, but blocky textures are also observed. Chlorite is also almost ubiquitous, occurring both as fibres and radiating bladed growths along the dilatant zones localized along the grain boundary and grain triple junctions (Fig. 5f).

FLUID INCLUSION ANALYSIS

Quartz veins collected from the Duke of York Island (Fig. 1) were selected because textural relationships between the veins and the host rocks are very evident and the effects of transposition due to D1 are less developed, allowing a more complete description of the overall structural fabric.

Quartz crystals hosted in the three different vein sets (category *a*, *b* and *c*; samples CR1-11/01/02, CR2-11/01/02, and CR3-11/01/02, respectively, in Table 1) contain abundant fluid inclusions, all suitable for microthermometric analyses. Based on phase numbers at room temperature two types of fluid inclusions were recognized, hereafter referred as type *I* and type *II*, respectively. Type *I* consists of monophase, gas (pure N_2, see below) inclusions and were found only in the CR1-11/01/02 samples (category *a* veins). They occur both in clusters redistributed along subgrain boundaries and along intragranular trails. Their dimension ranges from 5 to 25 μm (Fig. 6a,b). Type *II* consists of two-phase, L + V fluid inclusions. Type *IIa* (the most abundant) consists of regular shaped, two-phase L-rich inclusions, which occur in all the vein categories (Fig. 6c). In particular, they occur in the least deformed samples along closely spaced, subparallel, transgranular healed microfractures, producing a texture similar to a crack-seal microstructure (Ramsay, 1980). Type *IIb* consists of re-equilibrated L + V, L-rich inclusions. A wide range of re-equilibration textures has been observed in the samples. No solids within the two types of fluid inclusions have been observed. Type *II* inclusions are highly variable in size. They range from 10 to 12 μm for the smooth preserved type *IIa* inclusions, and up to 80 μm for the biggest, exploded type *IIb* inclusions (considering the halos and the satellite inclusions) (Fig. 6d,e).

In CR1-11/01/02 samples (category *a* veins), type *I* gas-bearing inclusions are spatially associated with type *II*, L + V fluid inclusions. This argues for their simultaneous trapping and immiscibility between the two fluid phases during the quartz deposition (see also Lewis *et al.*, 2000). Trails of type *II* fluid inclusions are also observed with mutual overprinting relationships, but usually intragranular. These textural observations suggest either a primary or a pseudosecondary origin for the fluid inclusion types hosted in category *a* veins.

A huge number of type *II* fluid inclusions is hosted in quartz crystals of the CR2-11/01/02 samples (category *b* veins). These inclusions show different sizes and shapes, and it is very difficult to determine their origin and timing of entrapment. Many of the fluid inclusions show re-equilibration textures (type *IIb*) and decrepitated exploded inclusions, together with some annular and/or semi-annular shapes, were observed. Type *IIa* fluid inclusions also occur either isolated or along discordant annealed fractures that terminate within the quartz crystal margins.

In the CR3-11/01/02 samples, type *II* fluid inclusions are numerous, commonly occurring along healed microcracks. These inclusion trails often cross each other and the grain boundaries, attesting for a pseudosecondary or secondary origin (Fig. 6f). Primary, isolated-type *IIa* fluid inclusions are also present. Re-equilibration textures of fluid inclusions are less evident.

Microthermometry

Conventional freezing and heating microthermometric analyses were carried out according to the procedure outlined in the Appendix. To limit the possible effects caused by post-entrapment re-equilibration changes on

Fig. 4. Microphotographs illustrating characteristics of category *a* veins in sections cut parallel to the macroscopic lineation and orthogonal to the F1 fold axis (samples CR1-11/01/02 in Table 1). (a) Deformation features representative of both dissolution-precipitation creep and crystal plasticity in quartz grains (crossed polars). Pressure solution is evidenced by dissolution of quartz grains, together with truncation (T), overgrowth (O) and grain-to-grain indentation (I) microstructures. Plastic deformation in quartz is attested by patchy undulose extinction. A few grains display subgrains. (b) Domainal quartz-mica fabric induced by pressure solution (natural light). Activity of pressure solution is indicated by stylolitization of both quartz grains and mica seams. Note occurrence of intragranular, subvertical trails of healed fractures in the coarse-grained quartz grains. (c) Internal microstructures in coarse-grained quartz grains showing healed microfractures at high-angle to the dissolution seams (crossed polars). Overgrowth microstructures (O) indicative of pressure-solution are also found in association with interfacial free-energy polygonal textures (F). (d) Typical microstructure in quartz grains showing polygonal microfracture network associated with dissolution seams induced by pressure-solution (crossed polars). (e) Accumulation of small sub-angular quartz fragments surrounding coarse-grained quartz grains indicating microscale cataclasis (crossed polars). (f) Sutured intragranular contacts cut at high-angle by intragranular healed microfractures, indicative of vein filling by crack-seal processes (crossed polars). (g) Texturally late fracturing and brecciation of the quartz vein (crossed polars). Fracturing is mainly localized along grain triple junctions and calcite constitute the cement filling the voids. (h) Kinking of calcite and fracturing of both quartz and calcite (crossed polars). Morerover, note the moderate plastic deformation in the adjacent quartz grains.

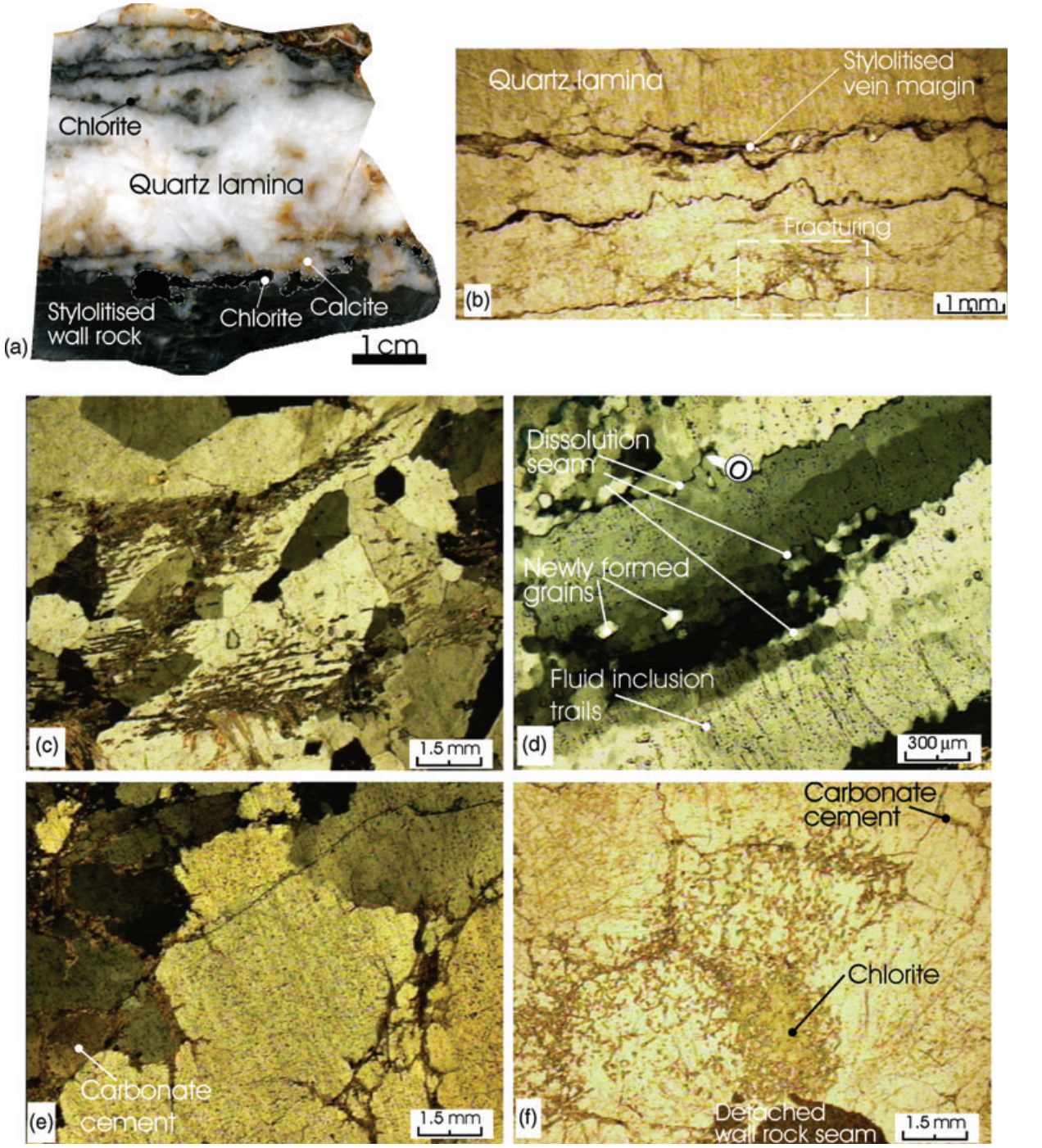

Fig. 5. Characteristics of categories *b* and *c* veins as seen in sections cut normal to macroscopic lineation and normal to vein surfaces (see Table 1 for sample locations). (a) Vein slab showing the banded nature of the quartz veins. Coarse-grained calcite grains are distributed within the vein and along the vein wall–rock interfaces. Chlorite overgrowth also rims the vein (sample CR2-24/01/02). (b) Thin section showing stylolitized elongated quartz laminae with the characteristic high length/width ratio (natural light; sample CR2-24/01/02). (c) Thin section showing preserved original microstructure indicative of vein filling by crack seal processes (crossed polars; sample CR8-21/01/02). These microstructures are only locally preserved. (d) Typical microstructures of coarse-grained quartz showing microstructures indicative of dissolution-precipitation creep, such as dissolution seams and overgrowth (O). Intragranular healed microcracks filled by fluid inclusions occur at high angle with respect to the dissolution seams. Note also the occurrence of newly formed tiny quartz grains produced during cataclastic microfracturing of the coarse-grained ones (crossed polars, sample CR2-24/01/02). (e) Fracturing of quartz grains filled with carbonate cement (crossed polars; sample CR3-11/01/02). (f) Coarse-grained porosity along quartz grain triple junctions sealed by carbonate cement and overprinted by texturally late chlorite crystallization (natural light; sample CR2-11/01/02).

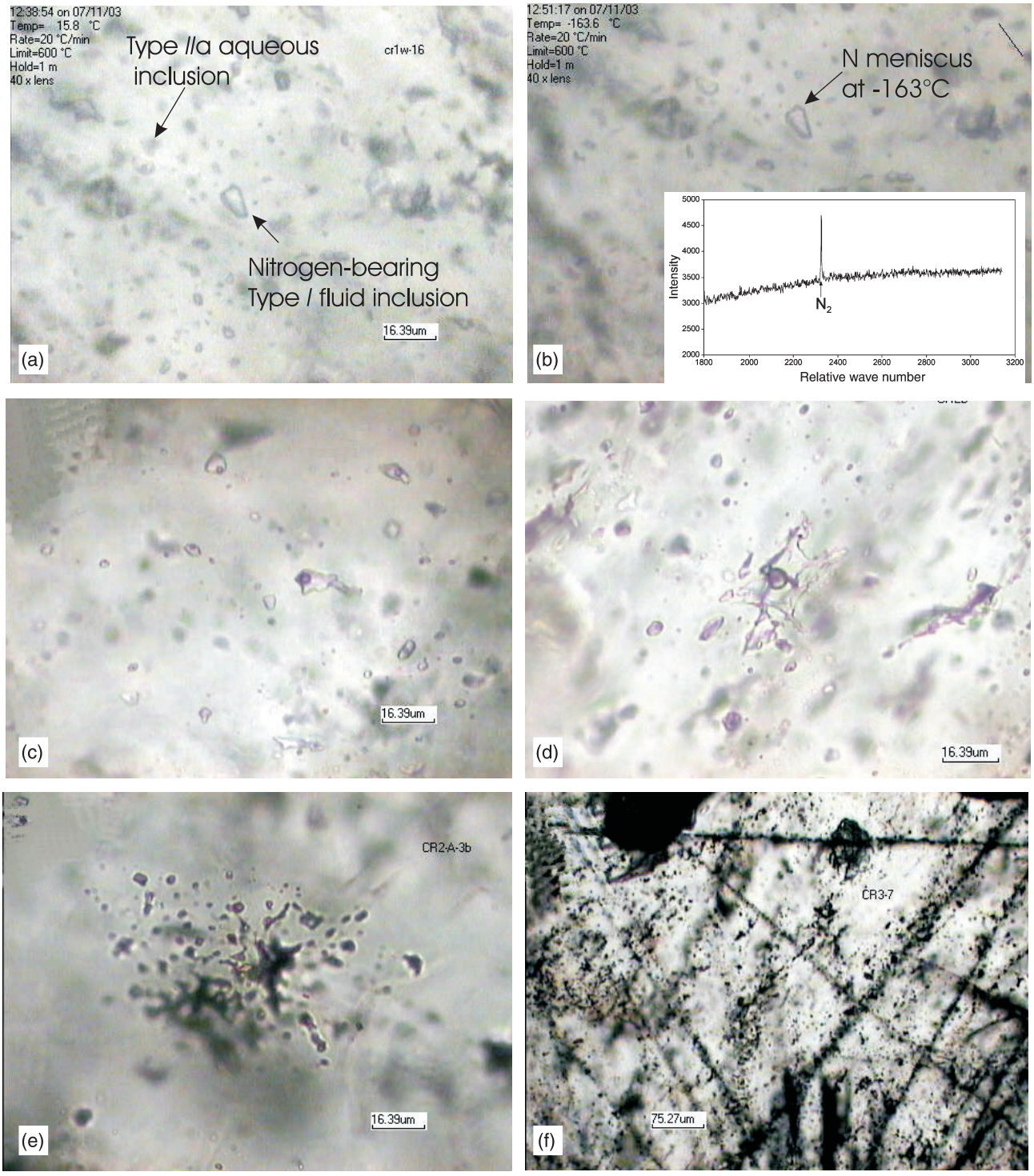

Fig. 6. Photomicrographs of different fluid inclusion types. (a) Type *I* nitrogen-bearing inclusions coexisting with type *IIa* aqueous inclusion at room temperature (sample CR1-11/01/02). (b) Type *I* nitrogen-bearing inclusions during freezing at −160 °C. Note the meniscus between liquid and vapour nitrogen. The Raman spectrum of the inclusion with the peak at 2326.7 cm^{-1} is also indicated. (c) Type *IIa* aqueous inclusions in category *b* veins (sample CR2-11/01/02). (d) Type *IIb* fluid inclusion in category *b* veins. Vapour phase contains dissolved CO_2, CH_4, N_2 (sample CR2-11/01/02). (e) Decrepitated type *IIb* fluid inclusion (sample CR2-11/01/02). (f) Intra- and intergranular healed microcracks filled by type *II* fluid inclusions in category *c* vein samples, mostly not suitable for microthermometric measurements (sample CR3-11/01/02).

fluid inclusion homogenization temperatures (e.g. Roedder, 1984), only type *I* and type *IIa* fluid inclusions were analysed.

Type *I* inclusions appear as monophase at room temperature. Freezing is not always attainable because of the temperature limit of the stage. Cooling of the samples permits the identification of a meniscus at temperatures between −160 and −180 °C. On warming, it disappears at temperatures between −150 and −147 °C, defining the gas as pure nitrogen (Fig. 6b). According to the classification based on the number of phase transitions between −193 and +31 °C and on the nature of final transitions of Van den Kerkhof (1988), the type *I* gas-bearing inclusions belong to type H1, as they show only one phase transition (liquid–vapour homogenization). In addition, few cases of E-type inclusions (*sensu* Van den Kerkhof, 1988) were observed, in which no second phase nucleates on cooling to −193 °C. This implies that the homogenization temperature is lower than the minimum temperature limit of the microthermometric equipment. Whether the meniscus fades away or the homogenization occurs to vapour or to liquid is sometimes controversial. Observed critical temperatures occur at −147 °C; some slightly lower temperatures (to −150 °C) may be related to density fluctuations around the critical density (Touret, 1982). A number of 11 T_h measurements concentrate *c*. −147 °C, the critical (or near critical) temperature for nitrogen. Some spreading around this value has been registered, but most of the data correspond to the critical temperature. About 70 Raman spectrometry analyses have been performed onto the monophase type *I* inclusions on which microthermometry was available (plus unmeasured others). These analyses confirm the nature of pure N_2-bearing fluid inclusions. One of the obtained spectra is reported in Fig. 6b, where a shifting of the peak position from 2331 to 2325 cm^{-1} is evident.

The microthermometric data for type *II* inclusions are reported in Fig. 7. No data of eutectic temperatures for this type of inclusions have been obtained, mostly because of the small size of the inclusions. In any case, no complex fluid system is suggested from the freezing temperature of the solution (not lower than −40 °C). The system is thus a H_2O/NaCl-dominated fluid. A summary plot of T_h *v.* T_m values shows a rather clustered distribution, which suggests an unique fluid population (Fig. 7a). The scattered distribution of T_h for type *IIa* inclusions hosted in veins of category *a* may be probably ascribed to the re-equilibration processes that occurred during progressive deformation. Data of final melting temperatures range from −4 to −1 °C (6.5 to 1.7 wt% NaCl equivalent), mostly concentrating between −2 and −1 °C. The same temperature range was obtained for the type *c* veins. These temperatures correspond to quite low salinity values of *c*. 3.4 ÷ 1.7 wt% NaCl equivalent. Raman spectrometry analyses carried out on type *IIb* fluid inclusions hosted in quartz grains of the vein categories *b* and *c*

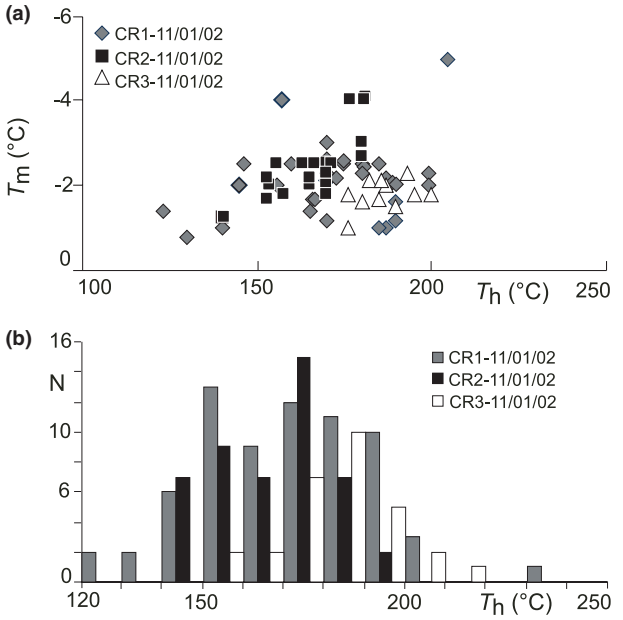

Fig. 7. (a) Plot of homogenization temperature (T_h) *v.* water ice melt temperature (T_m) for type *IIa* fluid inclusions from the three different vein categories. (b) Homogenization histogram for type *IIa* fluid inclusions from the three different vein categories.

also revealed the presence of gases in the bubbles, such as CO_2, CH_4 and N_2. Homogenization of the vapour and liquid phases to a single liquid phase for the CR1-11/01/02 samples gave values in a range of temperatures between 150 and 200 °C. The T_h histograms derived from CR2-11/01/02 and CR3-11/01/02 samples show more definite peaks, around the mean value of 180 °C (Fig. 7b).

STABLE OXYGEN-ISOTOPE ANALYSIS

Stable oxygen-isotope analyses were used to determine the sources of fluids that precipitated the minerals filling the veins and to trace the fluid–rock interactions in the vein system (e.g. Gray *et al.*, 1991; Evans & Battles, 1999; Cartwright & Buick, 2001; Richards *et al.*, 2002 and references therein). These analyses were performed on select samples of vein minerals (quartz and calcite), quartz and calcite grains from the host rock and the host rock itself. The results are listed in Table 4 (refer to Table 1 for sample locations). The analytical methods and the data reproducibility are described in the Appendix.

Despite the paucity of samples, the $\delta^{18}O$ values of quartz and calcite grains from the three vein generations show a close similarity (ranging from 15.22 to 16.90‰ and from 15.10 to 16.05‰, respectively), albeit the $\delta^{18}O$ values for the veins of category *a* are *c*. 0.5–1.5‰ lower than those of the other categories, with an average value of 15.30‰. The veins of category *b* and *c* show little dispersion around an average value of 16.08‰.

Table 4. Stable oxygen-isotope composition of quartz, calcite and host rock.

Sample veins	δ^{18}O(SMOW) ‰
Category *a*	
CR1-11/01/02 *qtz*	15.22
CR1-11/01/02 *qtz*	15.31
CR1-11/01/02 *cal*	15.10
CR1-13/01/02 *qtz*	15.38
Category *b*	
CR6-10/01/02 *qtz*	16.34
CR2-11/01/02 *qtz*	16.91
CR2-11/01/02 *cal*	15.38
CR2-12/01/02 *qtz*	16.9
CR2-12/01/02 *qtz*	16.88
CR2-12/01/02 *cal*	15.30
CR2-12/01/02 *cal*	16.05
CR2-12/01/02 *cal*	15.53
CR7-13/01/02 *cal*	14.15
CR7-13/01/02 *cal*	13.89
CR8-21/01/02 *qtz*	16.11
CR2-24/01/02 *qtz*	15.86
Category *c*	
CR3-11/01/02 *qtz*	16.71
CR3-11/01/02 *cal*	15.38
Host rock	
CR2-12/01/02 *w-r*	12.89
CR2-12/01/02 *w-r*	12.81
CR5-12/01/02 *w-r*	14.27
CR5-12/01/02 *cal*	15.46
CR5-12/01/02 *cal*	15.03
CR7-13/01/02 *w-r*	12.94
CR7-13/01/02 *w-r*	13.25
CR7-13/01/02 *qtz*	14.53
CR7-13/01/02 *qtz*	12.25
CR7-13/01/02 *qtz*	13.80
CR7-13/01/02 *qtz*	14.34
CR7-13/01/02 *qtz*	12.95

w-r, host rock; *cal*, calcite; *qtz*, quartz.

The host rock has of a wide range of lithologies (shale, siltstones, sandstones, graywackes and minor carbonates) and systematically provided isotopic compositions lower than those of the quartz veins, ranging from 12.81 to 14.27‰, with an average value of 13.23‰. Quartz grains extracted from the host rock show rather similar δ^{18}O values, ranging from 12.25 to 14.53‰, with an average value of 13.57‰. However, carbonates from the host rocks show a similar isotopic composition relative to the carbonate crystals precipitated in the veins, showing an average value of 15.25‰.

The vein–host rock relationships are shown in Fig. 8 on a plot of vein (quartz and calcite grains) δ^{18}O *v.* host-rock (including whole-rock, quartz and calcite fractions) δ^{18}O values. In this diagram, both quartz and calcite in veins exhibit clear isotopic disequilibrium relative to their host rock. In particular, the isotopic values of the veins result in a rather horizontal array, a distribution that is consistent with fluid-buffered, open-system behaviour (Gray *et al.*, 1991; Richards *et al.*, 2002). The oxygen-isotope compositions of calcite in veins and calcite in their coexisting host rocks fall along the diagonal line of the diagram, suggesting that all the carbonates, both deposited in veins and in the host rocks, re-equilibrated isotopically with the same oxygen reservoir.

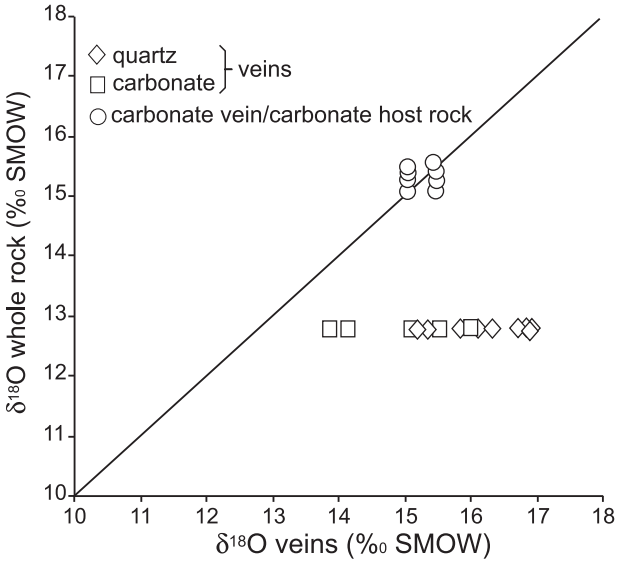

Fig. 8. Plot of host-rock δ^{18}O *v.* δ^{18}O composition of quartz and calcite in veins.

QUANTITATIVE CHEMICAL ANALYSES

Polished thin sections of selected samples of the vein–host rock contacts were analysed in order to evaluate: (i) composition of pressure-solution selvages in relation to the development and growth of veins (see Fisher *et al.*, 1995); and (ii) composition of the chlorite crystals hosted in veins, in order to infer the thermal conditions during the texturally late chlorite crystallization event in veins. Compositions were obtained using a CAMECA SX50 electron microprobe at the CNR laboratories of the University of Rome 'La Sapienza'. Beam conditions for these analyses were 15 kV and 12 nA, using natural minerals and synthetic phases as standards.

Host rock–vein chemical composition analyses

Following the procedure followed in Fisher *et al.* (1995), microprobe analyses were performed using a focused beam, rastering over an area of 100 μm × 90 μm. Compositional analyses carried out on profiles on either sides of two euhedral quartz growth veins (sample CR2-12/01/02; Table 1) document a strong depletion of silica around the veins (Fig. 9). Conversely, no significant variability in the Fe_2O/Al_2O_3 ratio is observed, which suggests that no long-distance mobility of these components occurred during pressure-solution and vein growth.

Chlorite composition and geothermometry

Standard microprobe analyses were performed on chlorite crystals, which are commonly found as a late-stage crystalline phase within the different sets of quartz veins. These chlorite analyses show a rather

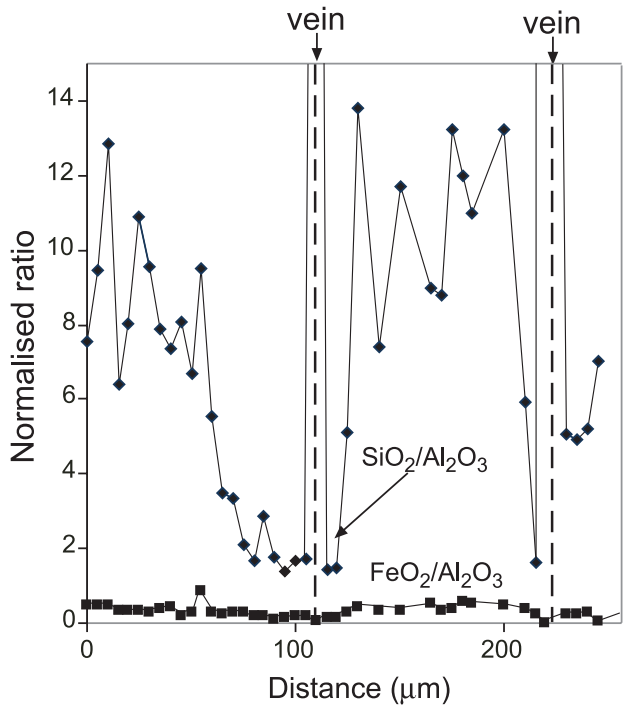

Fig. 9. Ratio of weight per cent SiO_2 and Fe_2O_3 normalized with respect to weight percent Al_2O_3, plotted as position with respect to two euhedral quartz growth veins. Note the significative SiO_2 depletion approaching the veins.

constant Fe/Mg ratio of 0.53 (Table 5), independent of the hosting vein category. Chlorite thermometry, based on the tenor of Al^{IV} substitution in the tetrahedral site (Chatelineau & Nieva, 1985), provided temperature estimates ranging from 330 to 340 °C, with no significant difference among the three vein categories (Table 5).

Table 5. Mean chemical composition analyses of chlorite hosted in the different vein generations.

	Category *a* veins	Category *b-c* veins
SiO_2	25.13	25.27
TiO_2	0.13	0.15
Al_2O_3	20	19.97
FeO	26.79	26.63
MnO	0.35	0.41
MgO	12.99	12.79
CaO	0.17	0.23
Na_2O	0.01	0.01
K_2O	0.23	0.31
Cr_2O_3	0.03	0.03
F	0.08	0
Total	85.91	85.88
Cations to 14 oxygen		
Si	2.74	2.76
Ti	0.01	0.01
Al	2.57	2.57
Fe^{2+}	2.45	2.43
Mn	0.03	0.04
Mg	2.11	2.08
Ca	0.02	0.03
Na	0	0
K	0.03	0.04
Cr	0	0
F	0.03	0.03
Total	10	9.99
X_{Fe}	0.53	0.53
Al^{IV}	1.27	1.24
T (°C)	342 ($n = 14$)	337 ($n = 21$)

The temperatures obtained with the thermometer of Chatelineau & Nieva (1985) are also shown (*n* corresponds to the number of analyses).

DISCUSSION

Progressive compressive deformation during vein system development

Quartz-bearing vein systems are common in chevron-folded, low-grade turbiditic sequences and have been ascribed to different phases of fold propagation and amplification (e.g. Tanner, 1989; Cosgrove, 1993; Jessel *et al.*, 1994). There are different opinions concerning the relevant model for vein formation in relation to folding and shearing. The controversy, in particular, concerns timing of vein with respect to fold development, i.e. pre- *v.* syn-folding models (see, e.g. Fowler, 1996). Nevertheless, hydraulic jacking apart of beds because of fluid overpressure either during sedimentary compaction (e.g. Henderson *et al.*, 1990) or early tectonic compression (Cosgrove, 1993) has been generally recognized as an effective mechanism leading to vein formation in compressive settings.

Overprinting relations reconstructed in the field, together with the microstructural characteristics support a continuum of deformation from pre-folding into the stage of fold amplification for the veins found in the Robertson Bay Terrane. This continuum of deformation is attested by the incremental development of the composite vein arrays with respect to the main foliation development (S1). Folding of lineated veins of the category *a* and their overprinting by pressure-solution cleavage unequivocally indicates a pre-folding origin. Veins of categories *b* and *c* systematically contain detached crenulated wallrock fragments and are, in turn, overprinted by pressure-solution cleavage. This suggests that they developed either during or after pressure-solution cleavage development in the wallrocks. Furthermore, microstructural evidence indicates that the deformation in quartz crystal was synchronous with pressure-solution differentiation and development of the S1 crenulation cleavage in the wallrocks.

The structural characters of the different quartz vein arrays also provide important information concerning their development during the progressive deformation of the Robertson Bay accretionary complex. The vein sets show strong analogies to the bedding-parallel, laminated quartz veins hosted in turbiditic sequences from the Palaeozoic Lanchlan Orogen of eastern Australia described by Jessel *et al.* (1994) and Fowler (1996). In particular, category *a* corresponds to their type 1 and categories *b* and *c* to their type 2. This evidence, coupled with: (i) the near-parallelism of the lineation trends within the three different vein groups and (ii) the systematic association with reverse shear

senses (Fig. 2f), indicate that the vein systems can be tentatively interpreted as bedding-parallel, thrust-related shear fractures (see also Cosgrove, 1993; Fowler, 1996), progressively overprinted during fold amplification and continuous shortening of the Robertson Bay Terrane.

Trapping conditions for fluid inclusions: fluid pressure cycling during deformation of the Robertson Bay Terrane

The microthermometric data obtained from the fluid inclusions hosted in quartz crystals growing during the development of the composite vein array (from category *a* to *c*) may be used to elucidate the *P–T* history associated with progressive deformation of the Robertson Bay accretionary complex.

Fluid inclusions (types *I* and *II*) hosted in the quartz grains in the early category *a* vein segregations provide insights into the density and pressure conditions of entrapment during the early phases of thrust faulting. Their occurrence in deformed samples suggests possible migration along subgrain boundaries during progressive deformation of quartz (e.g. O'Hara & Haak, 1992). This is confirmed by the arrangement of type *I* inclusions, mostly located along the grain boundaries, and by some scattering of T_h for type *II* inclusions (Fig. 7a), which indicates that pristine fluid densities have been slightly re-equilibrated during possible recovery processes associated with progressive deformation. Nevertheless, the occurrence of two immiscible fluid phases in category *a* veins (type *I* N_2-bearing and type *IIa* aqueous-dominated inclusions) permits the use of the isochore intersections method (Roedder, 1984) to provide constraints on the fluid *P–T* trapping conditions during formation of the Robertson Bay accretionary complex.

For the other samples, where there is no evidence for fluid immiscibility (veins of categories *b* and *c*), the fluid inclusions only provide the minimum trapping temperatures. However, clustering of T_h values around a mean value of 180 °C for all the inclusion types (independently from the hosting vein category) suggests rather similar trapping conditions. This is also confirmed by the grouping of the data in the T_h *v.* T_m plot (Fig. 7a) and by the presence of N_2 as an accessory phase in the type *II* fluid inclusions hosted in quartz grains from the category *b* veins. The T_h values can thus be considered as representative of the trapping conditions during progressive deformation and incremental shortening of the Robertson Bay Group rocks.

In the following, based on the pelite X-ray diffraction analyses, it is assumed that the range of probable background geothermal gradients for the Robertson Bay Group rocks was 25–30 °C km^{-1}. Lithostatic and hydrostatic thermobaric gradients are based on 27 and 10 MPa km^{-1} respectively (Fig. 10). From the peak temperature conditions inferred from the IC crystallinity data (*c.* 200–250 °C), maximum trapping

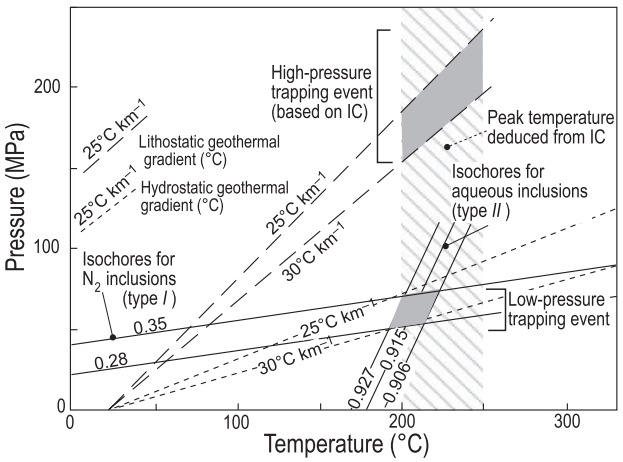

Fig. 10. Pressure–temperature diagram with isochores (numbers refer to calculated fluid densities in g cm^{-3}) for type *I*, N_2-bearing (homogenizing to liquid and to vapour) and aqueous, type *II* fluid inclusions derived from category *a* veins. Crossing of the two coeval immiscible fluids defines their trapping conditions. Also shown are lithostatic and hydrostatic thermobaric gradients based on geothermal gradients of 25 and 30 °C km^{-1}. Illite crystallinity (IC) thermometric data are also shown (see text for further details).

pressure for fluid inclusions ranges between 150 and 200 MPa under lithostatic and 50–70 MPa under hydrostatic conditions. The area in the *P–T* space defined by the intersections of isochores obtained from fluid inclusions hosted in quartz grains from veins of category *a* is consistent with a hydrostatic thermobaric gradient of 25–30 °C km^{-1} (Fig. 10). Accordingly, a minimum pressure difference of 80 MPa can be calculated by the two independent estimates (Fig. 10).

This pressure difference in trapping conditions may be the result of (Evans & Battles, 1999): (1) transient fluid pressure drops related to seismic pumping (Sibson *et al.*, 1975, 1988; Cox, 1995; Lewis *et al.*, 2000); or (2) real reduction of the stratigraphic overburden by erosion. The consistency in trapping temperatures for type *II* inclusions in the different vein sets, together with: (i) the evidence for an origin from a similar fluid composition, and (ii) the structural ground described in the previous section, suggest that fluid immiscibility was probably related to transient low-pressure conditions during stress-induced dilatation and continuous shortening (e.g. O'Hara & Haak, 1992; Robert *et al.*, 1995; Henderson & McCaig, 1996; Evans & Battles, 1999; Lewis *et al.*, 2000). Cyclically repeated pressure drops may have facilitated exolution of the nitrogen- (type *I*) and water- (type *II*) dominated fluids from a single starting fluid (Mullis, 1987; Vrolijk, 1987; Lewis *et al.*, 2000).

Therefore, transient fluid pressure conditions [from (supra)lithostatic to hydrostatic] during progressive deformation constitute the preferred mechanism for the observed pressure drop (see also O'Hara & Haak, 1992; Henderson & McCaig, 1996; Lewis *et al.*, 2000).

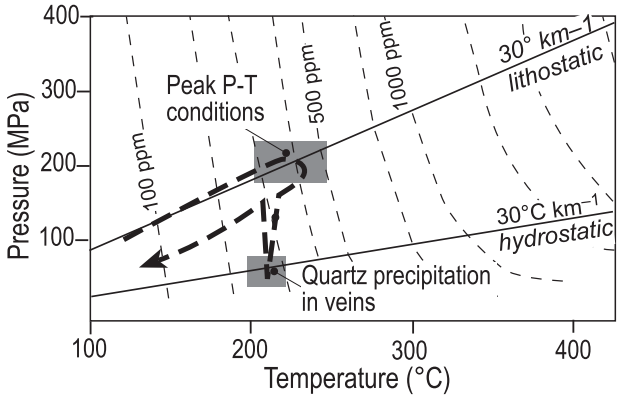

Fig. 11. Schematic pressure–temperature path illustrative of the *P–T* history described by the Robertson Bay Group rocks; solubility (in ppm) of quartz in water as a function of temperature and pressure is after Bons (2001), and references therein. Pressure fluctuations between lithostatic and hydrostatic conditions at *c*. 200 °C were primarily responsible for silica supersaturation and quartz precipitation in the vein network.

Accordingly, we propose that the achievement of the maximum burial at ~200 MPa was probably followed by the pressure drop induced by the pore pressure fluctuations accompanying shortening of the Robertson Bay accretionary complex. Quartz precipitation during vein segregation was thus a consequence of the oversaturation in Si following cyclically recurrent pressure drops during incremental compressive deformation (Fig. 11). In this interpretation, the gradient in the re-equilibration textures observed in type *II* fluid inclusions primarily records transient and fluctuating pressure conditions during the waning stage of the deformation and progressive exhumation of the Robertson Bay Group rocks.

Deformation processes and fluid-flow conditions during formation of the Robertson Bay accretionary complex

Microfabric of the quartz grains hosted in the different vein sets attests that progressive deformation during building of the Robertson Bay accretionary complex was primarily driven by dissolution–precipitation creep and by the simultaneous activation of microcracking and minor recovery along stressed grain boundaries (subgrain formation and deformation lamellae). In this scenario, fluid–rock interactions are dominated by the presence of distributed aqueous pore fluid along stressed grain boundaries, which is an essential prerequisite to accommodate the pressure-solution deformation cycle, involving dissolution, solution transfer and precipitation (e.g. Rutter, 1983; Etheridge *et al.*, 1984; Cox & Etheridge, 1989; den Brok, 1998; Renard *et al.*, 1999). In particular, the quartz microstructure is dominated by fluid-assisted fracturing as attested by the development of polygonal fracture networks synchronous with the development of the dissolution surfaces during the regional S1 cleavage development. This is evident as the sites of stress concentration during cleavage development are also the sites where the more intense deformation of the quartz grains occurs. This deformation style strongly resembles the channel-like structures induced by cataclastic solution creep during solution mass transfer in salt (den Brok *et al.*, 1998), suggesting that fluid-dominated brittle deformation assisted dissolution–precipitation creep. This rheological behaviour is in accordance with what is expected from the deformation mechanism map for quartz (e.g. Ranalli, 1995) at the low-temperature conditions (*c*. 200 °C) inferred for the progressive deformation of the Robertson Bay Terrane.

The filling textures in the studied vein sets are diagnostic of episodic histories of deposition, mainly assisted by crack-sealing/healing processes. This adds strength to the results derived from the fluid inclusion studies, arguing for the cyclic developmental sequence of the deformation during fluid pressure fluctuations from (supra)lithostatic to hydrostatic values (Sibson *et al.*, 1988), that we link to incremental porosity creation and destruction induced by microscale cataclasis, and by pressure-solution and cementation (crack-seal) respectively (see also Renard *et al.*, 2000). In this scenario, the permeability enhancement created by hydrofracturing following fluid pressure building up after crack-sealing (e.g. Cox, 1995; Sibson, 2004) probably induced the availability of greater amounts of fluids in the deforming rock volume, increasing efficiency of fracturing and working against plastic deformation and the localized tendency to pore space reduction by recovery and/or cementation during progressive deformation (e.g. Oliver, 1996; Wintsch & Yi, 2002). This is confirmed by: (i) the absence of notable deformation by dislocation creep in quartz grains, as attested by the preservation of free-face polygonal textures and by only limited evidence of recovery processes (Stöckert *et al.*, 1999); and (ii) the intensity of plastic deformation, that systematically decreases in conjunction with an increase in the intensity of brittle fracturing moving from category *a* to category *c* veins. The reconstructed deformation system is thus mainly characterized by dissolution–precipitation creep, modulated by stress- and strain-rate-dependent fluid pressure cycling, associated with local and regional permeability variations induced by the distribution and evolution of the fracture network during regional thrusting.

Various arguments document that the thrust-related fracture (fault) network acted as fluid conduits and controlled the fluid flow. The isotopic signature of the fluids trapped within the different vein sets indicates that fluid(s) had an isotopic composition in disequilibrium with that of the host rock, suggesting quartz vein precipitation from externally derived fluids. Fluid migration and circulation is also documented by the precipitation of quartz, in conjunction with the coeval dissolution of the carbonate components of the host rock, as attested by the presence of CO_2 in the

early-trapped type *II* fluid inclusions. This suggests the progressive cooling of migrating warm fluid(s) through the rock section, as during fluid(s) cooling, quartz, which has a progressive solubility tend to precipitate, whereas, carbonate minerals, which have a retrograde solubility, tend to be dissolved (see, e.g. Evans & Battles, 1999 and references therein). This is confirmed by the occurrence of calcite as the main cement-filling porosity created at the quartz grain boundaries in veins of categories *b* and *c*, providing further evidence for channelization of cooling calcite-bearing fluids in a system previously dominated by silica dissolution and precipitation (e.g. Renard *et al*., 2000). The regional dissolution of carbonate vein minerals as warm fluids progressed through the rock section is also consistent with the fact that the later trapped type *II* inclusions contain little CO_2, attesting a later fluid migration event when much of the carbonate was dissolved, thereby reducing available CO_2. Finally, the isotopic composition of the calcite in veins is similar to the calcite grains from the host rocks suggesting that some calcite grains in the host rocks were probably formed from the vein-forming fluids and represent an alteration halo induced in the surrounding rocks by quartz precipitation in veins (Cartwright & Buick, 2001).

Despite the evidence discussed above supporting an open-system behaviour for fluid transport during vein segregations, elemental mapping results within the solution cleavage selvages indicate a local source for silica precipitation in fibrous and euhedral quartz veins associated with the category *b* and *c* shear veins (see also Fisher *et al*., 1995), suggesting that it is not necessary to invoke long-distance transport of fluids (close-system behaviour). We thus propose that both fluid advection and diffusive mass transfer were operative for fluid–rock interaction and vein formation during the building up of the Robertson Bay accretionary complex (see also Gray *et al*., 1991; Evans & Battles, 1999; Richards *et al*., 2002). In particular, we infer that fluid–rock interaction involved a contribution of both: (i) externally migrating fluids that advectively moved through the rock section as the result of seismic pumping (Sibson *et al*., 1975) channelized by the thrust-related fracture network (tectonically driven fluids) and (ii) the host rocks to the geochemical signature of the different vein generations.

In this scenario, the origin of low-salinity fluids such as those found as inclusions in quartz grains hosted in the veins of the Robertson Bay Group may be probably found in dehydration and devolatilization metamorphic reactions involving hydrous minerals at depth in the hinterland of the subduction zones (e.g. Evans & Battles, 1999; Goldstein *et al*., 2005). The released volatiles (such as N as ammonium from clay minerals) are then reconstituted by up dip transport of exotic fluids in the forearc regions, reacting with the local rocks and the existing fluid reservoirs (e.g. Bebout, 1996; Sibson, 2004). Creation of fluid-flow pathways through thrust-related fracture and fault networks punctuated by events of hydrofracturing, pressure-solution/cementation and minor recovery, is thus here considered as the only viable mechanism for fluid transport from the hinterland to the foreland during the Early Palaeozoic Robertson Bay accretionary complex formation.

As a final point, it is worth noting that the regional palaeogeothermal conditions during deformation of the Robertson Bay accretionary complex were apparently outlasted by a thermal overprint, as recorded by the late-stage chlorite crystallization within the vein network. Such a thermal overprint attests to the passage of warm fluids, which were >110 °C above the regional background temperature. The thermal overprint recorded by the chlorite thermometry also indicates disequilibrium fluid venting restricted to the high-permeability channels provided by the pristine, thrust-related vein network. The origin of this late-stage fluid input is, at this point, a matter of speculation. We propose two possible scenarios. First, fluid venting accompanying the upward migration of deeply generated fluids linked to fluid redistribution in the forearc of subduction zones is expected in compressional tectonic regimes (Sibson, 2004). In this case, a thermal overprint affecting the already-structured accretionary wedge has to be taken into account. High geothermal environments in accretionary wedges was documented for the Cretaceous Shimanto accretionary wedge of Japan and referred to the subduction of young, thermally immature oceanic lithosphere (Sakaguchi, 1996; Lewis *et al*., 2000). The thermal overprint recorded by the last-stage mesothermal fluid circulation could be thus interpreted as the effect of oceanic subduction during the Early Palaeozoic orogenic construction at the Palaeo-Pacific active margin of Gondwana. Alternatively, hydrothermal fluid circulation and dispersion linked to the post-orogenic emplacement and cooling of the Devonian–Carboniferous Admiralty Intrusives could be also taken into account. In this interpretation, hydrothermal activity is dependent upon the interaction between a heat source, circulating fluids and permeable pathways related to high fracture density (Kurevitz & Karson, 1997), which substantiates reactivation of the early thrust-related fracture network.

Further investigations are thus necessary to solve this problem, but as far as the interpretation proposed, spatial and temporal permeability maintenance of the fracture network are required to account for the described fluid outflow within the Early Palaeozoic Robertson Bay Terrane.

CONCLUSIONS

Our study documents interdependence between fluid production, deformation, fluid-flow channelization, microdilatancy, and recovery/cementation during Early Palaeozoic accretionary complex formation at the palaeo-Pacific active margin of Gondwana. Fluid

assisted dissolution–precipitation creep is here recognized as the main operative deformation mechanism during accretionary complex formation, analogous to that documented for large portions of the crust in convergent margin settings (e.g. Cox & Etheridge, 1989; Fisher *et al.*, 1995; Schwartz & Stöckert, 1996).

The results presented in this study also suggest that the fate of fluids entering subduction zones at shallower crustal levels are under the control led by the rate-limiting mechanisms influencing: (i) the thrust-related fracture/fault network organization, which provides the background permeability structures for fluid channelization, (ii) the pressure-solution deformation cycle, which also plays an important role in controlling fault healing, overpressuring and slip (see also Renard *et al.*, 2000); and (iii) fracture permeability maintenance, accomplished by fault propagation and interaction at mesoscale, coupled with cataclastic flow at the microscale.

ACKNOWLEDGEMENTS

This paper is based on the field studies carried out during the 17th PNRA (Programma Nazionale di Ricerche in Antartide) campaign. Financial support was obtained from the PNRA project. We thank G. Caneva for coordinating the field activity and all the other participants to the Cape Hallet camp for helpful discussions and suggestions in the field. F. Storti partly participated in the field work. Electron microprobe analyses were carried out at the Istituto di Geologia Ambientale e Geoingegneria-CNR, Rome. M. Serracino is thanked for his help and kind assistance during electron microprobe analyses. M.L. Frezzotti is thanked for help during Raman spectrometry analyses. R. Funiciello and F. Salvini are thanked for their continuous encouragement and support. Comments and advice by P. Bons on an early version of the manuscript are acknowledged. Constructive and thoughtful revisions by G. Ranalli and D. Gray and the editorial advice of D. Brown contributed to improve the paper.

REFERENCES

Asprey, L. B., 1976. The preparation of very pure F_2 gas. *Journal of Fluorine Chemistry*, **7,** 359–361.

Bakker, R. J., 2003. Package FLUIDS 1. Computer programs for analysis of fluid inclusion data and for modelling bulk fluid properties. *Chemical Geology*, **194,** 3–23.

Bebout, G. E., 1996. Volatile transfer and recycling at convergent margins: mass balance and insights from high-P/t metamorphic rocks (overview). In: *Subduction Top to Bottom* (eds Bebout, G. E., Scholl, D. W., Kirby, S. H. & Platt, J.), *American Geophysical Union, Geophysical Monograph*, **96,** 115–127.

Bodnar, R. J. & Vityk, M. O., 1994. Interpretation of microthermometric data for H_2O-NaCl fluid inclusions. In: *Fluid Inclusions in Minerals: Methods and Applications* (eds de Vivo, B. & Frezzotti, M. L.), pp. 117–130, Short Course IMA, Pontignano, Siena.

Bons, P. D., 2000. The formation of veins and their microstructures. In: *Stress, Strain and Structure, A Volume in Honour of W D Means* (eds Jessell, M. W. & Urai, J. L.), *Journal of the Virtual Explorer*, Vol. 2. http://virtual explorer.com.au/2000/volume2/www/contribs/bons/index.html.

Bons, P. D., 2001. The formation of large quartz veins by rapid ascent of fluids in mobile hydrofractures. *Tectonophysics*, **336,** 1–17.

Bradshaw, J. D., Weaver, S. D. & Laird, M. G., 1985. Suspect terranes and Cambrian tectonics in northern Victoria Land, Antarctica. In: *Tectonostratigraphic Terranes of the Circum-Pacific Region* (ed. Howell, D. G.), *Circum-Pacific Conference for Energy and Mineral Resources, Earth Science Series*, **1,** 467–479.

den Brok, S., 1998. Effect of microcracking on pressure-solution strain rate: the Gratz grain-boundary model. *Geology*, **26,** 915–918.

den Brok, S., Zahid, M. & Passchier, C., 1998. Cataclastic solution creep of very soluble brittle salt as a rock analogue. *Earth and Planetary Science Letters*, **163,** 83–95.

Buggish, W. & Kleinschmidt, G., 1989. Recovery and recrystallisation of quartz and crystallinity of illite in the Bowers and Robertson Bay terranes (northern Victoria Land, Antarctica). In: *Geological Evolution of Antarctica* (eds Thompson, M. R. A., Crame, J. A. & Thompson, J. W.), pp. 155–159, Cambridge University Press, Cambridge.

Byerlee, J., 1993. Model for episodic flow of high pressure water in fault zones before earthquakes. *Geology*, **21,** 303–306.

Cartwright, I. & Buick, I. S., 2001. Fluid generation, vein formation and the degree of fluid-rock interaction during decompression of high-pressure terranes: the Schistes Lustrés, Alpine Corsica, France. *Journal of Metamorphic Geology*, **18,** 607–624.

Chatelineau, M. & Nieva, D., 1985. A chlorite solid solution geothermometer. *Contribution to Mineralogy and Petrology*, **91,** 235–244.

Cosgrove, J. W., 1993. The interplay between fluids, folds and thrusts during deformation of a sedimentary succession. *Journal of Structural Geology*, **15,** 491–500.

Cox, S. F., 1995. Faulting processes at high fluid pressures: an example of fault-valve behavior from the Wattle Gully Fault, Victoria Australia. *Journal of Geophysical Research*, **100,** 12841–12859.

Cox, S. F. & Etheridge, M. A., 1989. Coupled grain-scale dilatancy and mass transfer during deformation at high fluid pressures: examples from Mount Lyell, Tasmania. *Journal of Structural Geology*, **11,** 147–162.

Etheridge, M. A., Wall, V. J., Cox, S. F. & Vernon, R. H., 1984. High fluid pressures during regional metamorphism and deformation: implication for mass transport and deformation mechanism. *Journal of Geophysical Research*, **89,** 4344–4358.

Evans, M. A. & Battles, D. A., 1999. Fluid inclusion and stable isotope analyses of veins from the central Appalachian Valley and Ridge Province: implications for regional synorogenic hydrologic structure and fluid migration. *Geological Society of America Bullettin*, **111,** 1841–1860.

Ferraccioli, F., Bozzo, E. & Capponi, G., 2002. Aeromagnetic and gravity anomaly constraints for an early Palaeozoic subduction system of Victoria Land, Antartica. *Geophysical Research Letters*, **29,** 1406.

Findlay, R. H., 1986. Structural geology of the Robertson Bay and Millen terranes, northern Victoria Land, Antarctica. In: *Geological Investigations in Northern Victoria Land* (ed. Stump, E.), *American Geophysical Union, Antarctic Research Series*, **46,** 91–114.

Finn, C., Moore, D., Damaske, D. & Mackey, T., 1999. Aeromagnetic legacy of early Palaeozoic subduction along the Pacific margin of Gondwana. *Geology*, **27,** 1087–1090.

Fioretti, A. M., Visonà, D., Cavazzini, G. & Lombardo, B., 1997. In: Devonian magmatism: implications for the evolution of

Northern Victoria Land, Antarctica, and correlation with southeastern Australia and northeastern Tasmania. In: *The Antarctic Region: Geological Evolution and Processes* (ed. Ricci, C. A.), pp. 293–296. Terra Antarctica Publication, Siena.

Fisher, D. M., 1996. Fabrics and veins in the forearc: a record of cyclic fluid flow at depth < 15 km (overview). In: *Subduction Top to Bottom* (eds Bebout, G. E., Scholl, D. W., Kirby, S. H. & Platt, J.), *American Geophysical Union, Geophysical Monograph*, **96,** 75–90.

Fisher, D. M., Brantley, S. L., Everett, M. & Dzvonik, J., 1995. Cyclic fluid flow through a regionally extensive fracture network within the Kodiak accretionary prism. *Journal of Geophysical Research*, **100,** 12881–12894.

Flöttmann, T., Gibson, G. M. & Kleinschmidt, G., 1993. Structural continuity of the Ross and Dalamerian orogens of the Antarctica and Australia along the margin of the paleo-Pacific. *Geology*, **21,** 319–322.

Fowler, T. J., 1996. Flexural-slip generated bedding-parallel veins from central Victoria, Australia. *Journal of Structural Geology*, **18,** 1399–1415.

Frey, M. & Robinson, D., 1999. *Low Grade Metamorphism*. Blackwell, Oxford.

Gair, H. S., Sturm, A., Carryer, S. J. & Grindley, G. W., 1969. *The Geology of Northern Victoria Land*. Antarctic Map Folio Series, American Geographical Society, New York. Folio 12, Pl. XII.

GANOVEX Team, 1987. Geological map of northern Victoria Land, Antarctica, 1/500.000, Explanatory Notes. *Geologisches Jahrbuch*, **0B66,** 7–79.

Goldstein, A., Selleck, B. & Valley, J. W., 2005. Pressure, temperature, and composition history of syntectonic fluids in a low-grade metamorphic terrane. *Geology*, **33,** 421–424.

Gray, D. R., Gregory, R. T. & Durney, D. W., 1991. Rock-buffered fluid flow interaction in deformed quartz rich turbiditic sequences, eastern Australia. *Journal of Geophysical Research*, **96,** 19681–19704.

Guidotti, C. V. & Sassi, F. P., 1986. Classification and correlation of metamorphic facies series by means of muscovite b_0 data from low grade metapelites. *Neues Jarbuch Mineralogische Abh*, **153,** 363–380.

Henderson, I. H. C. & McCaig, A. M., 1996. Fluid pressure and salinity variations in shear-related veins, central Pyrenees, France: implications for the fault-valve model. *Tectonophysics*, **262,** 321–348.

Henderson, J. R., Henderson, M. N. & Wright, T. O., 1990. Water-sill hypothesis for the origin of certain veins in the Meguma Group, Nova Scotia, Canada. *Geology*, **18,** 654–657.

Hoffman, J. & Hower, J., 1979. Clay mineral assemblages as low grade metamorphic geothermometers: applications to the thrust faulted disturbed belt of Montana, USA. In: *Aspect of Diagenesis* (eds P. A. Scholle & P. R. Schluger), *SEPM Special Publication*, **26,** 55–79.

Jacobsen, R. T., Stewart, R. B. & Jahangiri, M., 1986. Thermodynamic properties of nitrogen from the freezing line to 2000 K at pressures to 1000 MPa. *Journal of Physical and Chemical Reference Data*, **15,** 735–909.

Jessel, M. W., Willman, C. E. & Gray, D. R., 1994. Bedding parallel veins and their relationships to folding. *Journal of Structural Geology*, **16,** 753–767.

Kleinschmidt, G., 1983. Trends in regional metamorphism and deformation in northern Victoria Land, Antarctica. In: *Antarctic Earth Sciences* (eds Oliver, R. L., James, P. R. & Jago, J. B.), pp. 119–122. Cambridge University Press, Canberra.

Kleindschmidt, G. & Skinner, D. N. B., 1981. Deformation styles in the basement rocks of north Victoria Land, Antarctica. *Geologishes Jarbuch*, **41,** 155–200.

Kleinschmidt, G. & Tessensohn, F., 1987. Early Palaeozoic westward directed subduction at the Pacific margin of Antarctica. In: *Gondwana Six: Structure, Tectonics and Geophysics* (ed. McKenzie, G. D.). *American Geophysical Union, Geophysical Monograph Series*, **40,** 89–105.

Kleinschmidt, G., Mazzoli, C. & Sassi, F. P., 1991. The pressure character of the low-grade metapelites from Robertson Bay Terrane and Bowers Terrane, northern Victoria Land, (Antarctica). *Memorie della Società Geologica Italiana*, **46,** 283–290.

Knight, C. L. & Bodnar, R. J., 1989. Synthetic fluid inclusions: IX. Critical PVTX properties of NaCl-H2O solutions. *Geochimica et Cosmochimica Acta*, **53,** 3–8.

Kübler, B., 1967. La cristallinité de l'illite et le zones tout à fait supérieures du métamorphisme. In: *Etages tectoniques, Colloque de Neuchatel, 1966* (ed. Scwaer, J. P.), pp. 105–121. A la Baconnière, Neuchatel.

Kurevitz, D. & Karson, J. A., 1997. Structural Settings of hydrothermal outflow. Fracture permeability maintained by fault propagation and interaction. *Journal of Volcanological and Geothermal Research*, **79,** 149–168.

Lanson, B., 1997. Decomposition of experimental X-ray diffraction patterns (profile fitting): a convenient way to study clay minerals. *Clays and Clay Minerals*, **45,** 132–146.

Lewis, J. C., Byrne, T. B., Pasteris, J. D., London, D. & Morgan, G. B., 2000. Early Tertiary fluid flow and pressure-temperature conditions in the Shimanto accretionary complex of south-west Japan: constraints from fluid inclusions. *Journal of Metamorphic Geology*, **18,** 319–333.

Merriman, R. J. & Kemp, S. J., 1996. Clay minerals and sedimentary basin maturity. *Mineralogical Society Bulletin*, **111,** 7–8.

Mullis, J., 1987. Fluid inclusion studies during very low-grade metamorphism. In: *Low Temperature Metamorphism* (ed. Frey, M.), pp. 162–199. Blackie and Son Limited, London.

O'Hara, K. & Haak, A., 1992. A fluid inclusion study of fluid pressare and salinity variations in the footwall of the Rector Branch thrust, North Carolina, U.S.A. *Journal of Structural Geology*, **14,** 549–589.

Oinuma, K., Shimoda, S. & Sudo, T., 1972. Triangular diagrams for surveying chemical compositions of chlorites. *Journal of the Tokio University*, **15,** 1–33.

Oliver, N. S. H., 1996. Review and classification of structural controls on fluid flow during regional metamorphism. *Journal of Metamorphic Geology*, **14,** 477–492.

Ramsay, J. G., 1980. The crack-seal mechanism for rock deformation. *Nature*, **284,** 135–139.

Ranalli, G., 1995. *Rheology of the Earth*, 2nd edn. Chapman & Hall, London.

Renard, F., Park, A., Ortoleva, P. & Gratier, J. P., 1999. An integrated model for transitional pressure solution in sandstones. *Tectonophysics*, **314,** 97–115.

Renard, F., Gratier, J. P. & Jamtveit, B., 2000. Kinetics of crack-sealing, intergranular pressure solution, and compaction around active faults. *Journal of Structural Geology*, **22,** 1395–1407.

Rey, J. P. H. & Kübler, B., 1983. Identification des micas des series sedimentaires par diffraction x a partir de la serie harmonique (001) des preparations orientees. *Schweizerische Mineralogische und Petrographische Mitteilungen*, **63,** 13–36.

Ricci, C. A., Talarico, F. & Palmeri, R., 1997. Tectonothermal evolution of the Antarctic Paleo-Pacific margin of Godwana: a northern Victoria Land perspective. In: *The Antarctic Region: Geological Evolution and Processes* (ed. Ricci, C. A.), pp. 213–218. Terra Antartica Publications, Siena.

Richards, I. J., Connelly, J. B., Gregory, R. T. & Gray, D. R., 2002. The importance of diffusion, advection, and host-rock lithology on vein formation: a stable isotpote study from the Palaeozoic Ouachita orogenic belt, Arkansas and Oklahoma. *Geological Society of America Bullettin*, **114,** 1343–1355.

Robert, F., Boullier, A. M. & Firdaous, K., 1995, Gold-quartz veins in metamorphic terranes and their bearing on the role of fluids in faulting. *Journal of Geophysical Research*, **100,** 12861–12879.

Roedder, E., 1984. *Fluid inclusions. Reviews in Mineralogy 12*. Mineralogical Society of America, Washington, 644 pp.

Roland, N. W., Läufer, A. L. & Rossetti, F., 2004. Revision of the terrane model of north Victoria Land (Antarctica). *Terra Antartica*, **11,** 55–65.
Rutter, E. H., 1983. Pressure solution in nature, theory and experiment. *Journal of the Geological Society, London*, **140,** 725–740.
Saffer, D. M. & Bekins, B. A., 1999. Fluid budgets at convergent plate margins. Implications for the extent and duration of fault zone dilation. *Geology*, **27,** 1095–1098.
Sakaguchi, A., 1996: High paleogeothermal gradient with ridge subduction beneath the Cretaceous Shimanto accretionary prism, southwest Japan. *Geology*, **24,** 795–798.
Sassi, F. P. & Scolari, A., 1974. The b_0 value of potassic white micas as a barometric indicator in low-grade metamorphism of pelitic schists. *Contribution to Mineralogy and Petrology*, **45,** 143–152.
Sharp, Z. D., 1990. In situ laser microprobe techniques for stable isotope analysis. *Chemical Geology*, **101,** 3–19.
Sibson, R. H., 2004. Controls on maximum fluid overpressure defining conditions for mesozonal mineralisation. *Journal of Structural Geology*, **26,** 1127–1136.
Sibson, R. H., Moore, J. & Rankin, A. H., 1975. Seismic pumping – a hydrothermal fluid transport mechanism. *Journal of the Geological Society, London*, **131,** 653–669.
Sibson, R. H., Robert, F. & Poulsen, K. H., 1988. High-angle reverse faults, fluid pressure cycling, and mesothermal gold-quartz deposits. *Geology*, **16,** 551–555.
Stöckert, B., Wachmann, M., Küster, M. & Bimmerman, S., 1999. Low effective viscosity during high pressure metamorphism due to dissolution-precipitation creep: the record of HP-LT metamorphic carbonates and siliciclastic rocks from Crete. *Tectonophysics*, **303,** 299–319.
Schwartz, S. & Stöckert, B., 1996. Pressure solution in siliciclastic HP/LT metamorphic rocks – constraints on the state of stress in deep levels of accretionary complexes. *Tectonophysics*, **255,** 203–209.
Tanner, P. W. G., 1989. The flexural-slip mechanism. *Journal of Structural Geology*, **11,** 635–655.
Touret, J., 1982. An empirical phase diagram for a part of the N_2-CO_2 system at low temperature. *Chemical Geology*, **37,** 49–58.
Underwood, B. M., Laughland, M. M. & Kang, S. M., 1993. A comparison among organic and inorganic indicators in diagenesis and low-grade metamorphism. Tertiary Shimanto Belt, Shikoku, Japan. In: *Thermal Evolution of the Tertiary Shimanto Belt, Southwestern Japan: An Example of Ridge Trench Interaction* (ed. Underwood, M. B.). *Geological Society of America Special Paper*, **273,** 45–61.
Van den Kerkhof, A. M., 1988. *The System* CO_2-CH_4-N_2 in Fluid Inclusions. Free University Press, Amsterdam, 206 pp.
Vrolijk, P., 1987. Tectonically driven fluid flow in the Kodiak accretionary complex, Alaska. *Geology*, **15,** 466–469.
Warr, L. N. & Rice, H. N., 1994. Interlaboratory standardization and calibration of clay mineral crystallinity and crystallite size data. *Journal of Metamorphic Geology*, **12,** 141–152.
Wintsch, R. P. & Yi, K., 2002. Dissolution and replacement creep: a significant deformation mechanism in mid-crustal rocks. *Journal of Structural Geology*, **24,** 1179–1193.

Received 9 June 2005; revision accepted 15 October 2005.

APPENDIX: ANALYTICAL METHODS

Clay mineral crystallinity

X-ray powder diffraction analysis was carried out using a Scintag Mod X1 X-ray system equipped with a solid-state Si detector at the Dipartimento di Scienze Geologiche, Roma Tre University. Step-scan diffraction data were acquired under CuKα radiation, at 40 kV and 45 mA. X-ray-oriented slides (<2 and 2–16 μm grain-size fractions) were prepared by the pipette-on-slide method, keeping the specimen thickness as constant as possible, within the range of 1–3 mg of clay per cm^2 of glass slide. Oriented air-dried samples were scanned from 1 to 48°2θ with a step size of 0.05°2θ and a counting time of 4 s. The presence of expandable clays was determined for samples treated with ethylene glycol at 25 °C for 15 h. Ethylene-glycol-solvated samples were scanned at the same conditions of air-dried aggregates in the range of 1–30°2θ. Diffraction peaks were analysed using the X-ray system-associated program by first removing a linear background level and then fitting them using a Pearson VII function.

Illite crystallinity measurements (IC), expressed as Kübler index (full width at half-maximum height of the illite 10-Å X-ray diffraction peak, measured on the <2 μm size fraction of air-dried clay specimen using CuKα radiation; Kübler, 1967), were obtained by interpolating the background under the peak by connecting the background on both sides of the peak and by using a profile-fitting method (Lanson, 1997). All data presented in this paper were calibrated to the Crystalline Index Standard (CIS) scale of Warr & Rice (1994). Experimental values were converted to the standardized CIS values by the linear regression equation:

$$\text{Calibrated (CIS) data} = [\text{uncalibrated data (IC)} \times 2.0769] + 0.086 \quad (1)$$

Fluid inclusions

Microthermometry

Doubly polished sections of *c.* 200 μm of the study samples were analysed. A freezing–heating stage Linkam THMSG600 was used to perform the microthermometric measurements at the Istituto di Geologia Ambientale e Geoingegneria-CNR, Rome. The calibration of the stage was made using pure natural CO_2 inclusions for low temperatures and synthetic fluid inclusions for high temperatures. Reproducibility of the triple point of CO_2 at −56.6 °C was ±0.1 °C. Low temperatures (T_m) were determined with a 0.5–1 °C min^{-1} rate, homogenization temperature (T_h) with a heating rate of 5 °C min^{-1}. Isochores were calculated using the FLUIDS software package (Bakker, 2003). The isochore represents the P–T conditions at constant volume as a function of an equation of state; we use the equation of state of Bodnar & Vityk (1994) and Knight & Bodnar (1989) for aqueous inclusions and the equation of state of Jacobsen *et al.* (1986) for nitrogen inclusions.

Raman microspectrometry

Raman spectra were collected using a Confocal Labram Multichannel microspectrometre of the Jobin-Yvon ltd at the Dipartimento di Scienze della Terra, Siena University. The 514.5 nm was used as excitation line by an Ar^+ ion laser.

Oxygen-isotope analysis

The analyses were performed at the laboratories of Mass Spectrometry at the Istituto di Geologia Ambientale e Geoingegneria-CNR, Rome. Oxygen isotope data of quartz samples were produced by laser fluorination (Sharp, 1990), reacting 1.5–1.8 mg fragments in a F_2 gas atmosphere. We employed a 15-W CO_2 laser operating at a wavelength of 10.6 m to irradiate the samples, and

pure fluorine desorbed at 290 °C from hexafluoropotassium–nickelate salt (Asprey, 1976) as a reagent. The O_2 produced during laser fluorination was purified of excess fluorine and transferred to a cold finger with a 13 Å molecular sieve. Further oxygen gas purification was achieved by desorbing oxygen from the molecular sieve at *c.* −110 °C using a liquid nitrogen–ethanol mixture. The purified gas was then transferred to a Finnigan Delta + Mass Spectrometer for oxygen isotope analysis. The laboratory standard, calibrated against NBS 28 standard, was measured several times during the analysis session. Its standard deviation after 18 repetitions is equal to 0.08. Small aliquots of powdered calcium carbonate were used to perform the oxygen-isotope analysis. The automatic device Finnigan Kiel II carried out the extraction of CO_2. The calcium carbonate reacted in purified phosphoric acid (H_3PO_4) at 72 °C until all carbonate was completely digested; the resultant CO_2 was purified of contaminant water vapour and then analysed on a Finnigan Mat 252 mass spectrometer. Results are generally reproducible to $\pm 0.1‰$ or better.

The oxygen isotopic compositions are reported in per mil (‰) relative to the standard mean oceanic water (SMOW). All data are reported in delta notation, that represents the deviation of the sample with respect to a standard in part per mil, according to the following equation:

$$\delta = 1000 \times (R_{\text{sample}}/R_{\text{standard}} - 1), \quad (2)$$

where R is the heavy isotope/light isotope ratio.